Investigation of aerosol indirect effects using a cumulus microphysics parameterization in a regional climate model

Kyo-Sun Sunny Lim[1], Jiwen Fan[1], L. Ruby Leung[1], Po-Lun Ma[1], Balwinder Singh[1], Chun Zhao[1], Yang Zhang[2], Guang Zhang[3], and Xiaoliang Song[3]

[1]Pacific Northwest National Laboratory, Richland, Washington, USA

[2]North Carolina State University, Raleigh, North Carolina, USA

[3]Scripps Institution of Oceanography, La Jolla, California, USA

December 2013

Corresponding author address

Kyo-Sun Sunny Lim

Pacific Northwest National Laboratory, Richland, WA

E-mail: kyo-sun.lim@pnnl.gov

This article has been accepted for publication and undergone full peer review but has not been through the copyediting, typesetting, pagination and proofreading process which may lead to differences between this version and the Version of Record. Please cite this article as doi: 10.1002/2013JD020958

Abstract

A new Zhang and McFarlane (ZM) cumulus scheme includes a two-moment cloud microphysics parameterization for convective clouds. This allows aerosol effects to be investigated more comprehensively by linking aerosols with microphysical processes in both stratiform clouds that are explicitly resolved and convective clouds that are parameterized in climate models. This new scheme is implemented in the Weather Research and Forecasting (WRF) model, which is coupled with the physics and aerosol packages from the Community Atmospheric Model version 5 (CAM5). A test case of July 2008 during the East Asian summer monsoon is selected to evaluate the performance of the new ZM scheme and to investigate aerosol effects on monsoon precipitation. The precipitation and radiative fluxes simulated by the new ZM scheme show a better agreement with observations compared to simulations with the original ZM scheme that does not include convective cloud microphysics and aerosol-convective cloud interactions. Detailed analysis suggests that an increase in detrained cloud water and ice mass by the new ZM scheme is responsible for this improvement. Aerosol impacts on cloud properties, precipitation, and radiation are examined by reducing the primary aerosols and anthropogenic emissions to 30% of those in the present (polluted) condition. The simulated surface precipitation is reduced by 9.8% from clean to polluted environment and the reduction is less significant when microphysics processes are excluded from the cumulus clouds. Generally, cloud top height does not change significantly but the total cloud fractions are reduced by the increased aerosols due to suppressed convection, except during some heavy precipitation periods when cloud fraction, cloud top height, and rain rate are increased due to enhanced convection.

1. Introduction

The summer monsoon over East Asia brings abundant rainfall over China, Japan, and Korea, which can be characterized by deep convective systems that accompany the southwesterly flow of warm and moist air across the South China Sea toward those regions. The intensity of the East Asian summer monsoon (EASM) changes at inter-annual and multi-decadal time scales [*Lau et al.,* 2000]. One of the noticeable patterns of rainfall anomaly that emerged during the past half century over China is the so called “southern flood and northern drought” pattern [*Xu*, 2001; *Hu et al*., 2003] with increasing precipitation over the middle-lower valley of Yangtze River and decreasing precipitation in northern China. Coincidentally during the same time period, aerosol number concentration has significantly increased over China since the 1960s [*Luo et al*., 2001; *Guo et al*., 2011]. The positive increasing trends in AOD occur mostly in the aerosol source regions where high annual mean AOD is noticeable in the recent 10 years from 2000 to 2010 [*Luo et al*., 2013] largely due to rapid increases in anthropogenic aerosol emissions [*Ohara*, 2007].

Many recent observational studies have linked aerosol effects to changes in Asian monsoon and rainfall [e.g., *Lau and Kim*, 2006; *Bollasina et al*., 2008; *Lei et al*., 2011]. *Lei et al*. [2011] analyzed observation and reanalysis data and found that increasing anthropogenic aerosols could contribute substantially to the recent southern flood and northern drought trend over China. *Lau and Kim* [2006] suggested that an increased loading of absorbing aerosols over the Indo-Gangetic Plain during the pre-monsoon season could induce subsequent increased rainfall over the Indian subcontinent, and decreased rainfall over East Asia in June – July. *Bollasina et al*. [2008] also showed that excessive absorbing aerosols over South Asia in May could lead to reduced cloud amount and precipitation due to lower tropospheric heating, but increase monsoon strength and precipitation over India

later, particularly in June – July. The aforementioned studies have identified a couple of different pathways for how aerosols affect monsoon rainfall through interactions with both clouds and radiation, thus modulating the large-scale atmospheric circulation. In summary, aerosol impact on monsoon water cycle is extremely complex, and strongly depends on aerosol distribution and chemical characteristics, and varies at different spatial and temporal scales [*Lau and Kim*, 2006].

Driven by land-sea thermal contrast, the Asian monsoon is sensitive to many large-scale factors such as sea surface temperature (SST), snow cover, and soil moisture [*Lau et al*., 2008]. These factors are influenced by natural climate variability such as El Niño–Southern Oscillation (ENSO) and anthropogenic climate forcing from greenhouse gases and aerosols. Attributing observed changes in the monsoon to aerosols is very difficult because the signature of aerosol effects on the monsoon can be masked or modulated by other factors. Global and regional climate models are useful tools for assessing aerosol impact on the monsoon as they can be used to test different hypotheses of how aerosols can affect the monsoon system, once they are adequately evaluated using observations. *Guo et al.* [2013] performed such simulations to investigate the regional changes of rainfall caused by anthropogenic aerosols over the EASM region and found that the responses of the monsoon circulation to sulfate and black carbon emissions are different in different monsoon seasons. Similarly, global climate models such as the Geophysical Fluid Dynamics Laboratory (GFDL) model (CM3.0) and the Community Atmosphere Model version 5 (CAM5) were used to evaluate aerosol impacts on the South Asian monsoon [*Bollasina et al*, 2011; *Ganguly et al*., 2012]. A regional climate model with chemistry, such as the Weather Research and Forecasting (WRF) model with Chemistry (WRF-

Chem), was also utilized to examine aerosol impact on precipitation during the EASM [*Wu et al*., 2013] and a significant impact of aerosols on the precipitation shift from south to north was found. However, a significant limitation of all the models described above is that they only include representations of the interactions between aerosols and stratiform clouds. Therefore, they cannot simulate aerosol indirect effects (AIE) through convective clouds that are critically important in the EASM regime in which deep convective cloud systems dominate.

For deep convective clouds, aerosols in the polluted environment could invigorate convection by releasing additional latent heat from freezing of a greater amount of liquid due to delayed warm rain processes, which has been regarded as the driving force for the invigoration of convective clouds [*Rosenfeld et al*., 2008]. However, many cloud-resolving model studies have found both enhancement and suppression of precipitation by aerosols, depending on environmental conditions and cloud system types [e.g., *Khain et al*. 2005; *van den Heever et al*. 2006, 2011; *Tao et al*. 2007; *Fan et al*., 2009, 2012a; *Khain*, 2009; *Lim and Hong,* 2012]. *Fan et al*. [2012b] suggested that the significant latent heat from deep convection and large radiative forcing induced by aerosols could impact large-scale circulation. On the other hand, aerosol radiative effect could stabilize the atmosphere by enhancing the lower tropospheric heating [*Chung et al*. 2002; *Menon et al*. 2002; *Fan et al*. 2008]. Both aerosol radiative and indirect effects should be included at the cloud scale to comprehensively represent aerosol impacts. Limited by computational resources, convection must be parameterized in global and regional climate models that are applied at grid resolution of 10 km or coarser. However, the cumulus parameterizations commonly used in global and regional climate models do not

include cloud microphysics, so AIE through convective cloud processes cannot be considered.

Recently, *Song and Zhang* [2011] developed an efficient two-moment microphysics parameterization for convective clouds and implemented it in the Zhang and McFarlane (ZM) cumulus parameterization scheme [*Zhang and McFarlane*, 1995]. This new microphysical approach for the cumulus parameterization makes it possible to link aerosol with the parameterized convective cloud processes. This microphysics parameterization treats mass mixing ratios and number concentrations of four hydrometeor species (cloud water, cloud ice, rain and snow), and adopts several processes based on *Morrison and Gettelman* [2008] with modifications to suit convective clouds.

The purpose of this study is to investigate AIE on monsoon rainfall over eastern China in a regional climate modeling framework, and analyze the effects of microphysics processes in a cumulus parameterization scheme. Through implementation of the new ZM scheme into a regional climate model, we can investigate the aerosol impacts on both parameterized and grid-resolved clouds. The WRF-Chem model, which has been extensively used for regional climate [*Qian et al*., 2009; *Zhao et al.,* 2011, 2012; *Yang et al*., 2012; *Wu et al*., 2013] as well as air quality studies [*Grell et al.,* 2005; *Fast et al.,* 2006; *Zhang et al.,* 2010, 2012, 2013; *Chuang et al.,* 2011], has been modified and utilized for the present work. This paper is organized as follows. Section 2 describes the implementation of the new ZM scheme into the WRF model with experimental setup. Results and summary are presented in sections 3 and 4, respectively.

2. Model Descriptions

2-1. The original and new ZM schemes

The detailed formulation of microphysics in the ZM scheme is well described in *Song and Zhang* [2011]. Here, only the most noticeable differences between the original and new ZM schemes are delineated. The key improvements of the ZM scheme are (i) explicit treatment of hydrometeors including cloud liquid water and cloud ice for convective clouds, (ii) explicit calculation of precipitation rate from convections, and (iii) treatment of liquid and ice water (both mass and number) detrainment. We elaborate these improvements in the following description.

The budget equations of cloud water mixing ratio for the original and new ZM schemes are shown in Eq. (1-1) and (1-2), respectively. In the original ZM scheme, there is no separation between cloud liquid water (q_C) and cloud ice (q_I), which is simply treated as cloud water (q_W).

$$\frac{\partial}{\partial z}\left(M_U q_W\right) = -D_U q_W + C_U - C_0 M_U q_W \qquad (1\text{-}1)$$

$$\frac{\partial}{\partial z}\left(M_U q_{C,I}\right) = -D_U q_{C,I} + C_U + \frac{M_U}{W_U} S^q_{C,I} \qquad (1\text{-}2)$$

Here, M_u and D_u represent the convective updraft mass flux and detrainment rate, respectively, and W_u indicates the updraft vertical velocity. C_u and C_0 in Eq. (1-1) are the net condensation rate and conversion ratio from cloud water to precipitation, respectively. $S^q_{C,I}$ in Eq. (1-2) represents several microphysical source/sink terms for q_C or q_I per unit cloud area. C_0 in the original ZM scheme is computed using the empirical formulation by *Lord* [1982], which is a constant value and highly tunable. *Yang et al.* [2013] found that C_0 in the original ZM scheme is a very important parameter for the ice/liquid water path and cloud/radiation properties

from CAM5 experiments. The cumulus parameterization schemes implemented in the WRF model (Version 3.4.1) adopt different values of C_0. For example, the Grell-Devenyi [*Grell and Devenyi*, 2002] and Simplified Arakawa-Schubert cumulus schemes [*Arakawa and Schubert*, 1974; *Han and Pan*, 2011] use a value of 0.002 and the ZM cumulus scheme prescribes values of 0.0059 over land and 0.0450 over ocean.

Surface precipitation in the cumulus scheme is calculated as a vertical integral of precipitation production (PRD) rate considering the evaporation of PRD into the environment at each layer. The PRD rates in the original and new ZM schemes are shown below, respectively.

$$\text{PRD} = C_0 M_u q_w - EVP \tag{2-1}$$

$$\text{PRD} = \frac{M_u}{w_u} S_{R,S}^q - EVP \tag{2-2}$$

The first term in Eq. (2-1) and (2-2) is the conversion rate from cloud water to precipitation in the updraft and the second term, *EVP*, is the evaporation rate of precipitation under the assumption that downdrafts are maintained in a saturated state by evaporation. $S_{R,S}^q$ in Eq. (2-2) represents the microphysical source/sink terms for mixing ratios of rain (q_R) or snow (q_S). For example, S_R^q includes autoconversion, accretion of cloud water by rain, and accretion of rain by snow, heterogeneous and homogeneous freezing, and sedimentation. The new ZM scheme calculates the PRD rate through physically based microphysics parameterization relative to the original ZM scheme in which the PRD rate is based on the simple conversion ratio of C_0, commonly used in most cumulus schemes.

Another major difference between the original and new ZM schemes lies in the treatment of convective detrainment of cloud water. In the original ZM scheme, there

is no separation between cloud liquid water and cloud ice. Therefore, the detrainment rates of cloud liquid water and cloud ice mass from the ZM scheme are calculated using the total cloud water by multiplication of a factor that depends on temperature. In addition, the detrained number concentration of cloud water is diagnosed based on its mass and predefined droplet radius such as 8 μm for cloud liquid water and 25 μm for cloud ice in the original ZM scheme. The new ZM scheme treats detrainment based on the calculated mass and number concentrations of cloud liquid water and cloud ice from the microphysics parameterizations for convective clouds. The budget equations for number and mass concentrations together with their source/sink terms are presented in detail in *Song and Zhang* [2011]. The steady-state hydrometeor budget equations in the new ZM scheme are integrated from cloud base to cloud top due to the strong updrafts of convective clouds. The lower boundary conditions of cloud liquid water and cloud ice are calculated from the condensation/deposition and detrainment in the lowest layer above the boundary. The lower boundary conditions of rainwater and snow are calculated from their source, that is autoconversion from cloud liquid water and cloud ice. Meanwhile, the budget equations of rainwater and snow are integrated from model top to model bottom in the *Morrison and Gettelman* [2008] microphysics scheme by setting the upper boundary condition as zero, assuming weak vertical velocity over the stratiform clouds region. Note that the ZM cumulus scheme uses a steady-state convective updraft plume model [*Zhang and McFarlane*, 1995]. To keep consistency between the cumulus parameterization method and microphysics parameterization method in the new ZM scheme [*Song and Zhang,* 2011], budget equations of hydrometeors in the new ZM scheme are based on the steady-state budget equation, thus all hydrometeors are calculated in a diagnostic manner. The

net generation of cloud liquid water and cloud ice in each time step will be completely detrained into large-scale environment and therefore ensure the mass conservation.

2-2. Implementation of the new ZM scheme in WRF

The new ZM cumulus scheme with cloud microphysics parameterization is implemented into the WRF-Chem model. All the cloud microphysics processes in the new ZM scheme implemented into WRF-Chem are the same as *Song and Zhang* [2011]. Here, we briefly introduce the cloud droplet activation, ice nucleation, and freezing processes. For cloud droplet activation, the method of a lognormal aerosols size distribution developed by *Abdul-Razzak and Ghan* [2000] is adopted. Ice nucleation and freezing processes in the new ZM cumulus scheme follow the method in *Morrison and Gettelman* [2008] except for the immersion freezing process. Ice nucleation for cirrus clouds is based on *Liu and Penner* [2005]. For mixed-phase clouds, the condensational/ depositional nucleation is calculated based on *Meyers et al*. [1992]. Contact freezing follows *Cotton et al*. [1986] and *Young* [1974]. Immersion freezing in the new ZM cumulus scheme is calculated following *Diehl and Wurzler* [2004], but in the Morrison and Gettelman microphysics scheme it is calculated following *Bigg* [1953]. In our implementation, the detrainment process is modified from *Song and Zhang* [2011], which is described in Section 2.1. When temperature is warmer than $-5℃$, all existing cloud ice is converted to cloud liquid water.

The mass tendencies from cloud droplet activation and ice nucleation are included as a part of condensation from water vapor to cloud liquid water and deposition from water vapor to cloud ice in the new ZM scheme, respectively. Thus, the effects of cloud droplet activation and ice nucleation on temperature are

considered as part of the condensation and deposition processes, respectively. In the new ZM scheme, the net condensation rate, which is the sum of condensation rate and deposition rate, is calculated based on the assumption that the air in the convective ensemble is saturated at the environmental temperature and pressure and all condensation occurs within the updrafts [*Zhang and McFarlane,* 1995]. Once the net condensation rate is calculated, the condensation rate and deposition rate are determined depending on the net condensation rate and temperature. If temperature is warmer than $0°C$, the net condensation rate is equal to the condensation rate; if temperature is colder than $-35°C$, the net condensation rate is equal to the deposition rate. Otherwise, the deposition rate linearly increases when the temperature is between $-35°C$ and $0°C$.

2-3. WRF-CAM5 and Experimental Design

A variant of the WRF model version 3.4.1 [*Skamarock et al*., 2008] with chemistry (WRF-Chem) [*Grell et al*., 2005] that includes the CAM5 physics suite [*Neale et al*., 2010] is employed in this study. The CAM5 physics package was implemented by *Ma et al*. [2013a] into WRF to explore the performance of the global model parameterization suite at meso- and cloud-resolving scales [*Ma et al.,* 2013a; *Gustafson et al*., 2013]. Following a similar strategy to use WRF as a testbed for evaluating global climate model parameterizations for regional scale simulations, we choose the CAM5 physics package for our simulations, which includes both deep [*Zhang and McFarlane*, 1995] and shallow cumulus schemes [*Park and Bretherton*, 2009], the University of Washington turbulence scheme [*Bretherton and Park*, 2009], a two-moment microphysics scheme [*Morrison and Gettelman*, 2008], a simplified macrophysics scheme based on the CAM5 macrophysics [*Neale et al*., 2010], and a

3-mode (Aitken, Accumulation, and Coarse) modal aerosol module (MAM3) [*Liu et al*., 2012a] coupled with the gas phase chemistry of Carbon Bond Mechanism version Z (CBMZ) [*Zaveri and Peters*, 1999]. In MAM3, all aerosol species within each mode are assumed internally mixed. Aerosol optical properties are described in *Ghan and Zaveri* [2007]. The major microphysical interactions between clouds and aerosols are from droplet nucleation, scavenging, and re-suspension. The detailed model description for the CAM physics in WRF and evaluation are documented in *Ma et al*. [2013a]. The deep cumulus scheme is replaced by the new ZM scheme described in Section 2-2. For the land surface and radiation processes, which are not included in the implemented CAM5 physics package, we use the Noah land surface model [*Chen and Dudhia*, 2001], and the rapid radiative transfer model for global circulation models (RRTMG) shortwave and longwave radiation [*Mlawer et al*., 1997; *Iacono et al*., 2003, 2008] schemes that include aerosol radiative feedback [*Zhao et al.,* 2011]. The RRTMG radiative transfer schemes adopt the maximum-random overlap assumption to calculate cloudiness [*Collins*, 2001].

Emission data are generated based on the regional emission inventory for East Asia developed by Argonne National Laboratory [*Streets et al*., 2003, 2005; *Zhang et al*., 2007]. The meteorological initial and boundary conditions are derived from the NCEP Reanalysis 2 data [*Kanamitsu et al*., 2002]. The boundary condition for aerosols is provided by a previously performed offline CAM5 simulation [*Ma et al.,* 2013b] in which the model's wind, temperature, and surface pressure are prescribed by reanalysis dataset but aerosols and water substances are allowed to evolve freely. The simulation from the Model for Ozone and Related chemical Tracers (MOZART) version 4 [*Emmons et al.,* 2010] provides the boundary condition of trace gases. For the model lower boundary, the optimally interpolated SST (OISST) on a

1° × 1° grid is used. The weekly OISST is linearly interpolated in time to derive daily values during the integration period. Due to prescribed lateral boundary conditions from NCEP Reanalysis 2 data, there is no feedback from the WRF simulations to large-scale circulation. The experiments are performed for 37 days starting at 0000 UTC on 23 June 2008 during the EASM season. The simulation period is chosen to coincide with the U.S. Department of Energy Atmospheric Radiation Measurements (ARM) Mobile Facility AMF-China field campaign investigated by *Fan et al.* [2012a]. The first 7 days are regarded as a model spin-up period and are not included in the analysis. A domain with a 36-km grid resolution and 45 vertical layers is used to cover major parts of East Asia (Fig. 1).

To investigate the effects of microphysics processes in the ZM cumulus scheme, we designed two different simulations: one that uses the new ZM scheme with microphysics (hereafter “MP”) and the other that employs the new ZM scheme but with microphysics turned off (hereafter “NOMP”). In the NOMP experiment, cloud water and precipitation production processes including the detrainment treatment as described in Section 2-1 are replaced by the formulations from the original ZM scheme. By comparing these two experiments, the effect of cloud microphysics in the cumulus scheme on the simulated regional climate can be evaluated. It is noted here that both MP and NOMP use the present day emissions and meteorological fields. To examine aerosol effects on simulated precipitation during the monsoon season, we conduct an additional sensitivity experiment (hereafter “MP_Clean”). In the MP_Clean experiment, primary aerosols and gaseous species such as sulfur dioxide and nitrogen monoxide are reduced by 70% of their original values to mimic the relatively clean environment in East Asia prior to the rapid economic development in the last few decades. The simulation results are analyzed for one

month of July 2008 over the eastern part of China, where most rainfall is concentrated and aerosol emissions are greater than other places.

3. Results

3-1. Effect of microphysics in a cumulus scheme

Accumulated precipitation over the analysis domain during the month of July 2008 from the China Merged precipitation Analysis (CMA) data based on a dense surface network of rain gauges and model simulation with the new ZM scheme (MP) are shown in Figures 2a and 2b, respectively. The CMA dataset was gridded at a 10-km resolution. Overall MP simulates the stationary monsoon rain band relatively well in both its intensity and location except in the northwestern part of the analysis domain where spurious precipitation is noticeable (Fig. 2c). This could be due to biases in the circulation since nudging of the large-scale wind fields in a test improved the results. We did not use the experiment with nudging since an important goal of this study is to examine aerosol effects but nudging will suppress potential circulation changes related to aerosol effects. Meanwhile NOMP fails to capture the observed monsoon rain band, simulating less precipitation, compared to CMA (Fig. 2d). The differences of the total surface precipitation between MP and NOMP are plotted in Figure 2e, along with those of the grid-resolved precipitation (Fig. 2f), which is calculated by the Morrison and Gettelman microphysics scheme based on grid cell mean (resolved) atmospheric variables, and the cumulus precipitation (Fig. 2g), which is calculated based on the ZM scheme for the parameterized (unresolved or subgrid) cumulus convection. The percentage of grid-resolved (i.e., stratiform) and unresolved (i.e., cumulus) precipitation amounts relative to the total precipitation amounts is 49 and 51%, respectively. The ratio of grid-resolved and cumulus

precipitation varies depending on the convective time scale in the cumulus scheme. A previous study also shows that the cumulus precipitation is sensitive to this parameter [*Yang et al*., 2013]. From a series of sensitivity tests, we found that a convective time scale of 1200 seconds adequately captures the selected monsoon rainfall in our modeling framework.

Generally, including cloud microphysics and AIE on cumulus clouds, MP produces more precipitation than NOMP (Fig. 2e). Furthermore, as indicated by the difference in time-averaged zonal wind fields at 850 mb between MP and NOMP, microphysics and AIE effects in MP could bring more moisture into the coastal region from the East China Sea resulting in increasing precipitation over the corresponding region, compared to NOMP. The area-averaged grid-resolved rain is increased by over 47% from NOMP to MP (Fig. 2f). Meanwhile, the cumulus precipitation in MP is enhanced in the major rain band but suppressed north of the rain band. Based on the spatial correlation between the simulated and observed precipitation (0.30 vs. 0.20 compared with CMA and 0.36 vs. 0.19 compared with Tropical Rainfall Measuring Mission (TRMM) Multi-satellite Precipitation Analysis (TMPA) [*Huffman et al*., 2007]) and root mean squared error (103.69 vs. 106.13 with CMA and 103.69 vs. 106.13 with TMPA), improved simulation of precipitation is found in MP relative to NOMP. This suggests that considering cloud microphysics and AIE in cumulus clouds may improve the simulation of monsoon rainfall (see Table 1).

Figure 3 shows the time series of surface rain rate, net shortwave (SW) flux at the surface, and outgoing longwave (LW) flux at the top of atmosphere averaged over the analysis domain. For verification, precipitation from TMPA and CMA and the radiative fluxes from Clouds and the Earth's Radiant Energy System (CERES) are used. In general, TMPA tends to retrieve intense precipitation events more frequently

than CMA. Even though both experiments, MP and NOMP, generally reproduce the observed distribution of rain rate, MP outperforms NOMP during the heavy precipitation periods (i.e., 3-6 and16-20 July). Although NOMP appears to perform better in terms of the simulated rain amount during the heavy precipitation event from 20 to 23 July, the precipitation distributions in both experiments are not in good agreement with the observation during this period. The convection event, which developed during the corresponding period, is initially triggered over the southeastern part of the domain at 1500 UTC on 20 July within a very local region (not shown) that cannot be easily parameterized in a regional-climate model framework. The simulated radiative fluxes from MP show a better agreement with the observed fluxes (Fig. 3b). The SW flux at the surface is reduced and the net downward LW flux at the top of atmosphere is enhanced significantly in MP compared to NOMP and agree much better with the observations. For the period when the shortwave flux is relatively lower, the difference in the simulated radiative fluxes between the two experiments is large and MP clearly matches better with CERES. Statistical skill scores of the time series of surface rain rate and radiative fluxes are also shown in Table 1. Overall improvement is shown with MP except for the positive bias of rain rate when statistical skill scores are calculated using the CMA data.

Overall, improvements in MP are found in the simulated rainfall and radiative fluxes. To understand what contributes to the improvements in MP, vertical profiles of total mixing ratio of cloud ice and cloud liquid water and detrained cloud ice and cloud liquid water mass, together with the microphysics budgets from the resolved stratiform clouds in a model grid are constructed (Figure 4). MP simulates significantly higher total cloud mass in both liquid (0.0085 g kg^{-1} vs. 0.0045 g kg^{-1})

and ice (0.0033 g kg^{-1} vs. 0.0026 g kg^{-1}) (Fig. 4a). Also, much more cloud liquid water and cloud ice are detrained from the convective clouds by the cumulus scheme (Fig. 4b), which serves as sources of cloud liquid and ice water for the grid-resolved stratiform clouds. As revealed in the microphysics budget analysis (Fig.4c), accretion of cloud liquid water by rain (Pracw) plays a key role in rain mass production and the enhanced accretion is the main factor responsible for the difference in surface precipitation between MP and NOMP. Together with Pracw, the four processes including auto-conversion of cloud liquid water to rain (Praut), evaporation of rain (Prevp), accretion of rain by snow (Pracs), and freezing of rain (Prfrz) are stronger in MP with cloud microphysics and AIE for cumulus clouds. In summary, the enhanced microphysical processes lead to more detrained cloud liquid water and cloud ice that is responsible for the enhanced grid-resolved surface precipitation in MP.

Although the increase in grid-resolved precipitation shown in Figure 2f can be explained by the microphysics effect discussed above, the reason for decreasing (increasing) total precipitation over the northern (southern) part of the analysis domain shown in Figure 2e is not clear. To answer this question, we divide the analysis domain into two sub-domains: sub-domain A (35-38 N, 117-120 E) with negative cumulus rainfall difference and sub-domain B (30-33 N, 117-120 E) with positive cumulus rainfall difference (Fig. 2g) between MP and NOMP. Vertical profiles of net convective mass flux and upward vertical velocity together with PRD rate are shown in Figures 5a-b for sub-domain A and Figures 5d-e for sub-domain B. First we note that there is a correspondence between the change of the cumulus rainfall and meridional moisture flux difference between MP and NOMP (see Figs. 2g and 2h). By considering microphysics and AIE in MP, the southern part (sub-domain

B) is moistened further but the northern part (sub-domain A) becomes dryer relative to NOMP. Correspondingly, we see smaller (larger) convective mass flux and vertical velocity in MP over sub-domain A (sub-domain B), relative to NOMP (Figs. 5a and d). These indicate that including microphysics and AIE in the new ZM scheme can lead to changes in the atmospheric circulation that results in changes in moisture flux. The difference between MP and NOMP produces a cyclonic circulation covering half of the analysis domain. Moistening in the southern part (i.e., sub-domain B) of east China explains the stronger convection and larger precipitation, and drying of the northern part (sub-domain A) explains the weaker convection and reduced precipitation in MP.

Corresponding to the differences in convection strength, PRD rate that depends on the convective updraft mass flux is reduced (enhanced) over sub-domain A (B) in MP compared with NOMP in Figures 5b and e. Consistent with Figure 4c that shows the microphysics budget from the Morrison and Gettelman microphysics scheme, accretion of cloud water by rain (Pracw) and by snow (Psacw) is the most efficient source for rain and snow production in the new ZM. Over sub-domain B, enhanced convection leads to more condensation and more rain generation by accretion of cloud water (cf., Figs 5c and f). This result suggests that the new ZM scheme can produce stronger rain band over the East Asian monsoon region where moisture is abundant, which is closer to observation.

Figure 6 shows the vertical profile of the total cloud fraction and the differences in time series of area-averaged cloud top height over the whole the analysis region. Cloud top is defined as the highest level where cloud ice mass exceeds at least 10^{-5} kg kg^{-1}, thus excluding shallow warm clouds from the cloud top calculation. MP simulates higher cloud fraction over all layers (Fig. 6a). More detrained cloud liquid

water and cloud ice are probably responsible for the higher cloud fraction in MP at high altitude. At the lower and middle levels, enhanced convective strength with more detrained cloud liquid water is responsible for the higher cloud fraction. Overall, the averaged cloud top height is also higher in MP from day 1 to 23 July, especially during the heavy precipitation periods of 3-6 and 16-20 July (Fig. 6b), which is likely associated with deep convective clouds. After 23 July when precipitation is light, indicating more dominant shallow or stratiform clouds, MP including cloud microphysics and AIE on cumulus clouds simulates relatively lower cloud top height compared to NOMP. Moreover, NOMP develops isolated strong convection storms in the north during this period, which is not observed in CMA (figure not shown). This likely contributes to the higher averaged cloud top height from day 23 to 31 in NOMP.

The radiative forcing due to microphysics effect, calculated from MP minus NOMP, is shown in Figures 7a and b. By including microphysics in the cumulus parameterization the SW flux at the surface is reduced and the net downward LW flux at the top of atmosphere is increased in MP compared to NOMP (c.f., Fig. 3b). The top of atmosphere (TOA) SW forcing is negative while the TOA LW forcing is positive. The increased cloud fraction as shown in Figure 6a should be a significant contributor. Due to the large contribution of negative SW forcing during daytime, the net TOA radiative forcing is about -16.9 W m^{-2} (see Figs 7a and b). At the surface, strong net cooling is induced by the SW negative forcing. Overall, the microphysics effects lead to warming in the atmosphere by up to +2.1 W m^{-2} due to the trapped LW and cooling at the surface by about −19.0 W m^{-2}, which could potentially impact the simulated regional circulation. It is noted that the LW warming at night is rather

small during the simulation period, suggesting that few lower- and middle-level clouds at night.

3-2. Effect of aerosols on regional precipitation

In this section, we investigate aerosol effects on regional precipitation by comparing two experiments, MP and MP_Clean. Both experiments produce similar spatial distributions of aerosol number concentrations (Figs. 8a and b), but aerosol concentrations are much higher in the industrial regions such as Shijiazhuang (38 N, 114.5 E) (3930 cm^{-3} vs. 2243 cm^{-3}) and Shanghai (31 N, 121.2 E) (3546 cm^{-3} vs. 1846 cm^{-3}) in MP due to much higher emissions (Fig. 8c). Shijiazhuang suffers from a high concentration of sulfate, a fine particulate matter originated mainly from coal consumption [*Peng et al*., 2002] and most cities in the northeastern part of China experience severe air pollution because of dust particles combined with industrial pollutants. During the analysis period, the area-averaged aerosol concentrations are 2186 cm^{-3} for MP and 1268 cm^{-3} for MP_Clean.

The spatial distribution of accumulated surface precipitation from MP_Clean is shown in Figure 8d. Under clean environment, the region of intense surface precipitation is broadened (cp. Figs. 2b and 8d). Precipitation reduction by aerosols is noticeable over most of the region, although an increase of precipitation is found along the coastal and northern part of the domain (Fig. 8e). Changes in both grid-resolved precipitation from grid-resolved clouds and cumulus precipitation from the parameterized cumulus convection are responsible for the precipitation reduction (Fig. 8f). Reduction of precipitation over the main monsoon rainfall region induces secondary circulation (not shown), which could increase moisture flux over the periphery of the major monsoon band, leading to enhancement of precipitation. In

the coastal areas, cumulus precipitation is enhanced by aerosols, which leads to an increase in the total precipitation. This is consistent with many cloud-resolving model studies that showed enhanced convection and precipitation from deep convective clouds by aerosols in moist environments [e.g., *Seifert and Beheng*, 2006; *Fan et al.,* 2007; *Tao et al*., 2007; *Khain,* 2009].

Figure 9a shows time series of relative changes in area-averaged rain rate between MP and MP_Clean. Overall, MP simulates a lower rain rate than MP_Clean. Consistent with the spatial distribution (Fig. 8f), this difference is contributed by both grid-resolved and cumulus rain. There are three main heavy precipitation events from day 3 to 6, day 16 to 20, and day 20 to 23, indicated by the three boxes in Figure 9a. At the early stage of each heavy precipitation event, MP produces a higher rain rate than MP_Clean. This is particularly clear for the events during 16-20 and 20-23. We focus our analysis on the convection cells developed during days 16-20 because the model fails to capture the veracity of the precipitation event after 20 July. For the early stage of the precipitation event on July 16-20, MP simulates stronger convections and sustains a longer duration of convection relative to MP_Clean. This results in more precipitation during July 16-18 from MP. This analysis suggests that increasing aerosol concentrations may have different effects on precipitation for heavier versus lighter precipitation events that may correspond to different types of clouds. Aerosol enhancing precipitation for deep moist storms by invigorating convection and inducing stronger cold rain processes, has been reported in many cloud resolving modeling studies and observations [e.g., *Zhang et al*., 2007; *Fan et al.,* 2012b; *Li et al.,* 2011; *Niu and Li*, 2012; *Tao et al*., 2012]. On the other hand, aerosols are found to reduce precipitation in warm and stratiform

clouds that generally produce light rain rates (i.e., drizzle) [*Ackerman et al*., 2004; *Fan et al.,* 2012a].

For more detailed analysis, we group the analysis period into three different regimes based on the precipitation characteristics, such as grid-resolved precipitation dominant (RP) regime, cumulus precipitation dominant (CP) regime, and intermediate (IM) regime. To do this, we calculate the ratio of cumulus precipitation amount to the total precipitation amount for each grid cell. If the ratio is higher (less) than 0.9 (0.1), we define the corresponding regime as a CP (RP) regime. The IM regime is defined for events with the ratio lying between 0.4 and 0.6. Time series of the percentage of grid cells that belongs to the most dominant region are plotted in Figure 9b. Interestingly the RP regime is most dominant in MP while the CP regime is more dominant in MP_Clean, especially during the heavy precipitation events, such as the events on July 3 to 6, July 16 to 20, and July 20 to 23. This indicates more parameterized cumulus precipitation is reproduced over the analysis domain during heavy precipitation events under the clean environment.

Vertical profiles of composited number concentrations and mass mixing ratios of cloud liquid water and cloud ice over the RP regime are shown in Figures 10. As shown in Figures 10a and b for the RP regime, from the clean to polluted cases, cloud droplet number concentration is increased but cloud water changes little. Cloud ice number concentration is generally increased in the heterogeneous freezing regime (i.e., -40 to 0^{o}C) but reduced above 12 km, probably due to the competition of heterogeneous freezing that suppresses homogeneous freezing of aerosols [*Liu et al.,* 2012b]. The reduced rain mixing ratio in the polluted case is because conversion from smaller cloud droplets to rain is less efficient due to the significant increase of cloud droplet number that reduces cloud drop size (Fig. 10c). Snow mixing ratio is

also reduced from MP_Clean to MP, which is caused by reduced accretion of rain with ice/snow due to the lower rain mixing ratio. Therefore, surface precipitation production is reduced under the polluted environment since both rain and snow mixing ratios in the clouds are reduced.

For the CP regime where deep convective clouds are dominant, increasing aerosols produce more cloud ice and liquid water. This enhances the detrained cloud water and ice mass in the cumulus-precipitation dominant regime (Fig. 11a). At the same time, the detrained cloud droplet and ice number concentrations are increased by 43% and 153% from the clean to polluted cases (Fig. 11b). The increased cloud droplet and ice number and mass mixing ratios by aerosols are consistent with cloud resolving model simulations for deep convective clouds [*Khain et al.,* 2005; *Wang,* 2005; *Cheng et al., 2007; Fan et al.,* 2007]. However, the increase of cloud mass could be underestimated by the CAM5 physics framework, since the total condensed water is diagnosed first based on the meteorological conditions before aerosol effects are considered and aerosol indirect effects only change the partitioning of the total condensed water between liquid and ice. The large increase of cloud droplet number reduces the sizes of cloud droplets and amplifies the cloud lifetime effects (i.e., clouds last longer due to reduced precipitation) in polluted environment. The mean effective radius of detrained cloud liquid water from the cumulus scheme is 13.0 μm for MP and 16.3 μm for MP_Clean, respectively.

As pointed out by *Song et al*. [2012], cloud ice mass production due to the freezing processes is enhanced under polluted environment for convective clouds. However, the effect of heating induced by the freezing processes on cumulus thermodynamics is not considered in the current version of the new ZM scheme. The temperature increase caused by freezing processes is added to the large-scale

temperature tendency rather than the plume to ensure moist static energy conservation within the current model framework. This warming added to the upper atmosphere would stabilize the large-scale environment in MP and suppress convections. Hence Figure 11c shows that the strength of upward motion decreases and the net convective mass flux is weakened below 6-km in MP. This results in a decrease of cumulus precipitation in the major rain band under the polluted environment. In theory, the latent heat from freezing processes should invigorate the plume and lead to stronger convection and precipitation [*Rosenfeld et al.,* 2008]. The invigoration of convection by aerosol indirect effects has already been demonstrated by many cloud resolving model studies [e.g. *Wang,* 2005; *Khain et al.,* 2005; *Fan et al.,* 2012a; *Lebo et al.,* 2012; *Tao et al.,* 2007, 2012]. Although invigoration of convection does not necessarily lead to enhanced precipitation since surface precipitation depends on the net effect of warm rain suppression, evaporative cooling, convection invigoration, and the complicated feedback between cloud and large-scale circulation, a more physical way considering the effect of latent heat from ice production processes on convection plume should be pursued in the future.

Figure 12 shows the time series of differences in domain-averaged cloud top height and total cloud fraction between MP and MP_Clean. Generally, cloud top height does not change significantly from MP_Clean to MP, except during some heavy precipitation periods i.e., day 4-6 and day 16-19, where significant increases of cloud top height are seen from the clean to polluted cases. Correspondingly, we find the net convective mass flux and vertical velocity are increased, accompanying with the increased rain rates (Fig. 9a) and cloud fraction (Fig. 12b) during these two periods. Therefore, enhanced convection should be one of the factors responsible

for the increased cloud top height and cloud fraction during those heavy precipitation periods. Another factor for the increased cloud fraction and cloud top height is the microphysical effects by aerosols, i.e., the much slower dissipation of deep convective clouds induced by much reduced ice particle size and fall velocity, as shown in *Fan et al.* [2013]. During other times, a reduction of cloud fraction is seen from MP_Clean to MP, due to the suppressed convection as discussed. The radiative forcing caused by aerosols indirect effect, calculated from MP minus MP_Clean, is shown in Figures 7c and d. Overall, there is a warming effect on the top of atmosphere (TOA) and at the surface during daytime, due to SW warming from the reduced cloud fraction. Heating the lower atmosphere induced by aerosol radiative effects could reduce relative humidity and stabilize atmosphere [*Fan et al.,* 2008; *Lau and Kim,* 2006]. A weak cooling is induced by aerosols in the atmosphere also during daytime due to increasing outgoing LW flux resulted from reduced cloud fraction (Fig. 7d). Also due to reduced cloud fraction, a slight cooling at the surface at nighttime is seen.

To examine the robustness of our findings, 10 ensemble simulations are conducted with different initial conditions sampled from 19 June to 28 June instead of 23 June used in the control simulation. Although the difference between the ensemble mean polluted (Ens_MP) and clean (Ens_MP_Clean) cases becomes weaker relative to the control simulation (cp. Figs. 13a and 8e), the signal of decreasing precipitation is still apparent from the clean to polluted environment except in the coastal areas. Compared to the simulation results with MP, Ens_MP lowers the statistical skill scores for the simulated spatial distribution of precipitation due to localized convective events developed from the perturbed initial condition. *Morrison and Grabowski* [2011] performed 240-member ensemble simulations to

investigate aerosol indirect effects on tropical deep convections and thermodynamic environment. They found that the ensemble spread of the radiative fluxes among different ensemble members under the same aerosol concentrations is large and this variability is caused by random fluctuations of individual deep convective events in terms of their strength and timing.

Another sensitivity experiment (hereafter NOMP_Clean) is performed for comparison with NOMP to examine aerosol effects on clouds and precipitation through grid-resolved stratiform clouds only. In NOMP_Clean, we mimic the clean environment in the same way as done for MP_Clean but exclude the microphysics processes in the ZM cumulus scheme the same way as performed for NOMP. Reduction in precipitation amount is also simulated under the polluted environment in NOMP. However, the reduction of precipitation under the polluted environment is less from NOMP_Clean to NOMP compared with that from MP_Clean to MP (cp. Figs 13b and 8e). The same is found for both grid-resolved and cumulus precipitation (cp. Figs 13c and 8f). In other words, by taking into account cloud microphysics and AIE in the parameterized cumulus clouds, the simulated precipitation is more sensitive to aerosols (leading to larger reduction). Figures 13c and 8f also reveal that the precipitation responses of the large-scale clouds to increasing aerosols are similar to those of parameterized cumulus clouds. This may be determined by the similar two-moment cloud microphysical processes employed for both cloud regimes.

In the experiments without microphysics in the ZM scheme (i.e., NOMP and NOMP_Clean), the detrained cloud from the cumulus parameterization is not affected by aerosols. Thus, the cloud lifetime effect in those experiments is not as strong as in the experiments that include microphysics. The difference in grid-

resolved stratiform precipitation between NOMP and NOMP_Clean is smaller than that between MP and MP_Clean. Thus, including aerosol impacts in convective clouds not only affect precipitation from the parameterized cumulus clouds, but also change the aerosol impact on precipitation from the grid-resolved stratiform clouds.

4. Summary and Discussion

We implemented the new ZM cumulus scheme that includes cloud microphysics in convection into the WRF model coupled with the physics package from the CAM5 (Version 5.1), and link the cloud droplet activation and ice nucleation processes in the convective clouds with aerosol properties predicted by MAM3. Microphysical process for convective clouds is treated based on *Morrison and Gettelman* [2008] with modifications to suit convective clouds in the new ZM scheme. This paper presents the first study to use this scheme in a regional climate model to examine the effects of including microphysics processes in the cumulus scheme on convective clouds and investigate the impacts of aerosols on the East Asian monsoon.

Both precipitation and radiative fluxes simulated by the new ZM scheme exhibit better agreements with the observed values during the East Asian monsoon season compared to the ZM scheme that does not include cloud microphysical processes and AIE in cumulus clouds. Our analysis suggests that increased detrained cloud water and cloud ice, which also result in higher cloud fraction and cloud top height especially during the heavy precipitation periods, are responsible for this improvement. In addition, the microphysics processes in the new ZM scheme lead to a radiative warming in the atmosphere, which potentially affects the simulated regional-scale circulation. A consistent treatment of microphysics in both convective

and stratiform clouds is a major strength of this modeling approach. *Song et al.* [2012] showed that this consistent treatment in CAM5 exhibited various improvements, which include reduction of large negative biases in cloud liquid water path over the subtropical ocean and better precipitation distribution.

Having demonstrated improvements from the new ZM scheme, we investigated aerosol effects on the East Asian monsoon with this new ZM scheme. Increasing aerosols from the clean to polluted environments generally reduces precipitation, because rain and snow particle formation becomes less efficient with the increased number of smaller droplets. Both precipitation from grid-resolved clouds and parameterized cumulus clouds are reduced. In addition to the less efficient production of rain and snow, another reason for the reduction of precipitation in cumulus clouds by aerosols is the weakened convection, indicated by the smaller updraft velocity and low-level convective mass flux. The following factors could contribute to the weakened convection: (1) the effect of latent heating induced by the freezing processes on cumulus thermodynamics is not considered in the current version of the new ZM scheme; (2) the latent heating from freezing and radiative warming added to the upper atmosphere under the polluted environment stabilizes the large-scale environment and suppress convection; and (3) aerosol radiative effects which could heat the lower atmosphere and reduce relative humidity, and stabilize atmosphere [*Fan et al.,* 2008; *Lau and Kim,* 2006]. However, it should be noted that during some heavy precipitation periods (such as Day 4-6 and Day 16-19), the increased aerosols enhances precipitation rates. A review study by *Tao et al.* [2012] concluded that increasing aerosol concentrations could either enhance or suppress precipitation processes and surface rainfall.

The increased aerosols do not change cloud top height significantly in general, except during some heavy precipitation periods, when significant increases of cloud top height are seen in the polluted case because of enhanced convection. A reduction of cloud fraction is seen most of the time due to the suppressed convection. Due to reduced cloud fraction from the clean to polluted environment, a warming effect at TOA and the surface is produced, accompanied by a weak cooling in the atmosphere during daytime. A slight cooling at the surface at nighttime is seen as well.

For warm-based deep convection clouds in this study, aerosols are likely invigorating convection by latent heat through the enhanced freezing processes based on conceptual theory [e.g., *Rosenfeld et al.* 2008] and observations [e.g., *Li et al.,* 2011] and numerous cloud resolving model simulations [e.g., *Khain et al.,* 2005; *Fan et al.,* 2012a,b]. Because the temperature increase caused by freezing processes is added to the large-scale temperature tendency rather than the plume in the new ZM scheme and CAM5 physics package, this warming in the upper atmosphere would stabilize the large-scale environment [*Song and Zhang*, 2011]. Therefore, the model is not able to simulate the convection invigoration due to aerosol increase. The choice to add the latent heat of freezing to the large-scale temperature tendency is necessitated by the need to conserve mass in the current cumulus scheme. However, this treatment has important effects so further investigation of approaches in parameterizing microphysics feedback to the dynamics should be pursued in the future to better simulate aerosol impacts on convective clouds while maintaining mass conservation and the saturation state of the updraft.

In our simulation, radiative forcing induced by aerosol is much smaller compared to the difference caused by microphysics effects of convective clouds alone (Fig. 7). We found that cloud model representation, especially the representation of microphysics processes for convective clouds in the cumulus scheme used in this paper, can significantly affect the simulated precipitation, radiative forcing, and atmospheric circulation at a regional scale. This microphysics effect is larger than the effect from increasing aerosols. Therefore, it is essential to take into account cloud microphysics and AIE in the parameterized cumulus clouds to better simulate regional climate. Because our study examines only a single summer month during the East Asian monsoon, further study is needed to more extensively evaluate the impacts of introducing cloud microphysics in cumulus parameterization and examine the role of aerosols in regional climate. Additionally, sensitivity to model resolution and different implementations of the parameterization such as related to the treatment of latent heating associated with microphysical processes in the temperature tendency discussed above should be pursued to improve understanding of the impacts of the new ZM scheme on the simulated climate.

Acknowledgement

This study was supported by the Office of Science of the U.S. Department of Energy as part of the Regional and Global Climate Modeling program through funding to PNNL and NCSU (DE-SC0006695). The Pacific Northwest National Laboratory is operated for DOE by Battelle Memorial Institute under contract DE-AC06-76RLO 1830. The first author would like to express her gratitude to Dr. Jin-Ho Yoon for his careful comments and encouragement during the preparation of this paper.

References

Abdul-Razzak, H., and S. J. Ghan (2000), A parameterization of aerosol activation: 2. Multiple aerosol types, *J. Geophys. Res.,* **105**(D5), 6837–6844, doi:10.1029/1999JD901161.

Ackerman, A. S., M. P. Kirkpatrick, D. E. Stevens, and O. B. Toon (2004), The impact of humidity above stratiform clouds on indirect aerosol climate forcing, *Nature,* **432,** 1014–1017, doi:10.1038/nature03174.

Arakawa, A., and W. H. Schubert (1974), Interaction of a cumulus cloud ensemble with the large-scale environment, *J. Atmos. Sci.*, **31**, 674–701.

Bigg, E. K., The formation of atmospheric ice crystals by the freezing of droplets, *Q. J. R. Meteorol. Soc.*, **79**, 510–519, 1953.

Bollasina, M., S. Nigam, and K.-M. Lau (2008), Absorbing aerosols and summer monsoon evolution over South Asia: An observational portrayal, *J. Clim.*, **21**, 3221–3239.

Bollasina, M. A., Y. Ming, and V. Ramaswamy (2011), Anthropogenic aerosols and the weakening of the South Asian summer monsoon, *Science*, **334**, 502–505.

Bretherton, C. S., and S. Park (2009), A new moist turbulence parameterization in the Community Atmosphere Model, *J. Clim.*, **22**, 3422–3448.

Chuang, M.-T., Y. Zhang, and Daiwen Kang (2011), Application of WRF/Chem-MADRID for Real-Time Air Quality Forecasting over the Southeastern United States, *Atmos. Environ.,* **45** (34), 6241-6250.

Chen, F., and J. Dudhia (2001), Coupling and advanced land surface-hydrology model with the Penn State-NCAR MM5 modeling system. Part I: Model implementation and sensitivity, *Mon. Weather Rev.*, **129**, 569–585.

Cheng, C.-T., W.-C. Wang, and J.-P. Chen (2007), A modeling study of aerosol impacts on cloud microphysics and radiative properties, *Q. J. R. Meteorol. Soc.,* **133,** 283–297.

Chung, C. E., V. Ramanatahn, and J. T. Kiehl (2002), Effects of the South Asian absorbing haze on the northeast monsoon and surface-air heat exchange, *J. Clim.*, **15**, 2462–2476.

Collins, W. D. (2001), Parameterization of generalized cloud overlap for radiative calculations in general circulation models, *J. Atmos. Sci*, **58,** 3224-3242.

Cotton, W. R., G. J. Tripoli, R. M. Rauber, E. A. Mulvihill (1986), Numerical simulation of the effects of varying ice crystal nucleation rates and aggregation processses on orographic snowfall, *J. Clim. Appl. Meteorol.*, **25**, 1658–1680.

Diehl, K., and S. Wurzler (2004), Heterogeneous drop freezing in the immersion mode: Model calculations considering soluble and insoluble particles in the drops, *J. Atmos. Sci.*, **61**, 2063–2072.

Emmons, L. K., et al. (2010), Description and evaluation of the Model for Ozone and Related chemical Tracers, version 4 (MOZART-4), *Geosci. Model Dev.*, **3**(1), 43–67.

Fan, J., R. Zhang, G. Li, and W.-K. Tao (2007), Effects of aerosols and relative humidity on cumulus clouds, *J. Geophys. Res.,* **112,** D14204, doi:10.1029/2006JD008136.

Fan, J., R. Zhang, W.-K. Tao, and K. I. Mohr (2008), Effects of aerosol optical properties on deep convective clouds and radiative forcing, *J. Geophys. Res.*, **113**, D08209, doi:10.1029/2007JD009257.

Fan, J., T. Yuan, J. M. Comstock, S. Ghan, A. Khain, L. R. Leung, Z. Li, V. J. Martins, and M. Ovchinnikov (2009), Dominant role by vertical wind shear in regulating aerosol effects on deep convective clouds, *J. Geophys. Res.,* **114,** D22206, doi:10.1029/2009JD012352.

Fan, J., L. R. Leung, Z. Li, H. Morrison, H. Chen, Y. Zhou, Y. Qian, and Y. Wang (2012a), Aerosol impacts on clouds and precipitation in eastern China: Results from bin and bulk microphysics, *J. Geophys. Res.,* **117,** D00K36, doi:10.1029/2011JD016537.

Fan, J., D. Rosenfeld, Y. Ding, L. R. Leung, and Z. Li (2012b), Potential aerosol indirect effects on atmospheric circulation and radiative forcing through deep convection, *Geophys. Res. Lett.,* 39, L09806, doi:10.1029/2012GL051851.

Fan, J., L. R. Leung, D. Rosenfeld, Q. Chen, Z. Li, J. Zhang, and H. Yan, 2013: Microphysical effects determine macrophysical response for aerosol impacts on deep convective clouds, *Proc. Natl. Acad. Sci. U. S. A.*, **110 (48),** E4581-E4590, doi: 10.1073/pnas.1316830110.

Fast, J. D., W.I. Gustafson Jr., R.C. Easter, R. A., Zaveri, J. C. Barnard, E.G. Chapman, G. A. Grell (2006), Evolution of ozone, particulates, and aerosol direct forcing in an urban area using a new fully-coupled meteorology, chemistry, and aerosol model, *J. Geophys. Res.,* **111**, D21305, doi:10.1029/2005JD006721.

Ganguly, D., P. J. Rasch, H. Wang, and J.-H. Yoon (2012), Climate response of the South Asian monsoon system to anthropogenic aerosols, *J. Geophys. Res.,* **117**, D13209, doi:10.1029/2012JD017508.

Ghan, S. J., and R. A. Zaveri (2007), Parameterization of optical properties for hydrated internally-mixed aerosol, *J. Geophys. Res.,* **112,** D10201, doi:10.1029/2006JD007927.

Grell, G. A., and D. Devenyi (2002), A generalized approach to parameterizing convection combining ensemble and data assimilation techniques, *Geophys. Res. Lett.*, **29**(14), 1693, doi:10.1029/2002GL015311.

Grell, G. A., S. E. Peckham, R. Schmitz, S. A. McKeen, G. Frost, W. C. Skamarock, and B. Eder (2005), Fully coupled "online" chemistry within the WRF model, *Atmos. Environ.*, **39**, 6957–6975.

Guo, J. P., X. Y. Zhang, Y. R. Wu, Y. Z. Zhaxi, H. Z. Che, B. La, W. Wang, and X. W. Li (2011), Spatio-temporal variation trevnds of satellite-based aerosol optical depth in China during 1980–2008, *Atmos. Environ.*, **45**(37), 6802–6811.

Guo, L., E. J. Highwood, L. C. Shaffrey, and A. G. Turner (2013), The effect of regional changes in anthropogenic aerosols on rainfall of the East Asian Summer Monsoon, *Atmos. Chem. Phys.,* **13,** 1521-1534, doi:10.5194/acp-13-1521-2013.

Gustafson, W. I., Jr., P.-L. Ma, H. Xiao, B. Singh, P. J. Rasch, and J. D. Fast (2013), The Separate Physics and Dynamics Experiment (SPADE) framework for determining resolution awareness: A case study of microphysics, *J. Geophys. Res. Atmos.*, **118,** doi:10.1002/jgrd.50711.

Han, J., and H.-L. Pan (2011), Revision of convection and vertical diffusion schemes in the NCEP global forecast system, *Weather Forecast,* **26,** 520–533.

Hu, Z., S. Yang, and R. Wu (2003), Long-term climate variations in China and global warming signals, *J. Geophys. Res.,* **108**, D194614, doi:10.1029/ 2003JD003651.

Huffman, G. J., R. F. Adler, D. T. Bolvin, G. Gu, E. J. Nelkin, K. P. Bowman, Y. Hong, E. F. Stocker, and D. B. Wolff (2007), The TRMM multisatellite precipitation analysis (TMPA): Quasi-global, multiyear, combined-sensor precipitation estimates at fine scales, *J. Hydrometeorol.*, **8**, 38–55.

Iacono, M. J., J. S. Delamere, E. J. Mlawer, and S. A. Clough (2003), Evaluation of upper tropospheric water vapor in the NCAR Community Climate Model (CCM3) using modeled and observed HIRS radiances, *J. Geophys. Res*., **108,** 4037, doi:10.1029/ 2002jd002539.

Iacono, M. J., J. S. Delamere, E. J. Mlawer, M. W. Shephard, S. A. Clough, and W. D. Collins (2008), Radiative forcing by long-lived greenhouse gases: Calculations with the AER radiative transfer models, *J. Geophys. Res*., **113,** D13103, doi:10.1029/2008jd009944.

Kanamitsu, M., W. Ebisuzaki, J. Woollen, S.-K. Yang, J. Hnilo, M. Fiorino, and G. Potter (2002), NCEP-DOE AMIP-II Reanalysis (R-2), *Bull. Am. Meteorol. Soc.*, **83**, 1631–1643.

Khain, A., D. Rosenfeld, and A. Pokrovsky (2005), Aerosol impact on the dynamics and microphysics of convective clouds, *Q. J. R. Meteorol. Soc.*, **131**, 2639–2663.

Khain, A. P. (2009), Notes on state-of-art investigations of aerosol effects on precipitation: A critical review, *Environ. Res. Lett.*, **4**, 015004, doi:10.1088/1748-9326/4/1/015004.

Lau, K. M., K. M. Kim, and S. Yang (2000), Dynamical and boundary forcing characteristics of regional components of the Asian summer monsoon, *J. Clim.*, **13**, 2461–2482.

Lau, K.-M., and K.-M. Kim (2006), Observational relationships between aerosol and Asian monsoon rainfall, and circulation, *Geophys. Res. Lett.,* **33,** L21810, doi:10.1029/2006GL027546.

Lau, K-M., and coauthors (2008), The Joint Aerosol-Monsoon Experiment: A new challenge for monsoon climate research, *Bull. Am. Meteorol. Soc.*, **89**, 369–383, doi:10.1175/BAMS-89-3-369.

Lebo, Z. J., H. Morrison, and J. H. Seinfeld (2012), Are simulated aerosol-induced effects on deep convective clouds strongly dependent on saturation adjustment?, *Atmos. Chem. Phys.*, **12**(20), 9941–9964.

Lei, Y. H., B. Hoskins, and J. Slingo (2011), Exploring the interplay between natural decadal variability and anthropogenic climate change in summer rainfall over China. Part I: Observational evidence, *J. Clim.,* **24,** 4584–4599.

Li, Z., F. Niu, J. Fan, Y. Liu, D. Rosenfeld, and Y. Ding (2011), Long-term impacts of aerosols on the vertical development of clouds and precipitation, *Nat. Geosci.*, **4**, 888–894.

Lim, K.-S. S., and S.-Y. Hong (2012), Investigation of aerosol indirect effects on simulated flash-flood heavy rainfall over Korea, *Metero. Atmos. Phys.* **118,** 199-214.

Liu, X., and Coauthors (2012a), Toward a minimal representation of aerosols in climate models: description and evaluation in the Community Atmosphere Model CAM5, *Geosci Model Dev.,* **5,** 709-739, doi: 10.5194/Gmd-5-709-2012.

Liu, X., X. Shi, K. Zhang, E. J. Jensen, A. Gettelman, D. Barahona, A. Nenes, and P. Lawson (2012b), Sensitivity studies of dust ice nuclei effect on cirrus clouds with the Community Atmosphere Model CAM5, *Atmos. Chem. Phys. Discuss.*, **12**, 13,119–13,160.

Liu, X., and J. E. Penner (2005), Ice nucleation parameterization for global models, *Meteorol. Z.*, **14**.

Lord, S. J. (1982), Interaction of a cumulus cloud ensemble with the large-scale environment. Part III: Semi-prognostic test of the Arakawa-Schubert cumulus parameterization, *J. Atmos. Sci.*, **39**, 88–103.

Luo, Y., X. Zheng, T. Zhao, and J. Chen (2013), A climatology of aerosol optical depth over China from recent 10 years of MODIS remote sensing data, *Int. J. Climatol.,* doi: 10.1002/joc.3728.

Luo, Y. F., D. R. Lu, X. J. Zhou, W. L. Li, and Q. He (2001), Characteristics of the spatial distribution and yearly variation of aerosol optical depth over China in last 30 years, *J. Geophys. Res.*, **106**(D13), 14,501–14,513.

Ma, P.-L., P. J. Rasch, J. D. Fast, R. C. Easter, W. I. Gustafson, X. Liu, S. J. Ghan, B. Singh (2013a), Assessing the CAM5 Physics Suite in the WRF Model: Model Implementation, Evaluation, and Resolution Sensitivity, *Geosci. Model Dev. Discuss.,* **6,** 6157-6218, doi:10.5194/gmdd-6-6157-2013,

Ma, P.-L., P. J. Rasch, H. Wang, K. Zhang, R. C. Easter, S. Tilmes, J. D. Fast, X. Liu, J.-H. Yoon, and J. F. Lamarque (2013b), The role of circulation features on black carbon transport into the Arctic in the Community Atmosphere Model version 5 (CAM5), *J. Geophys. Res. Atmos.*, **118**, 4657–4669, doi:10.1002/jgrd.50411.

Menon, S., J. Hansen, and L. Nazarenko (2002), Climate effects of black carbon aerosols in China and India, *Science*, **297**, 2250–2253.

Meyers, M. P., P. J. DeMott, and W. R. Cotton (1992), New primary ice-nucleation parameterization in an explicit cloud model, *J. Appl. Meteorol.*, **31**, 708–721.

Mlawer, E. J., S. J. Taubman, P. D. Brown, M. J. Iacono, and S. A. Clough (1997), Radiative transfer for inhomogeneous atmospheres: RRTM, a validated correlated-k model for the longwave, *J. Geophys. Res.*, **102**(D14), 16,663–16,682.

Morrison, H., and W. W. Grabowski (2011), Cloud-system resolving model simulations of aerosol indirect effects on tropical deep convection and its thermodynamic environment, *Atmos. Chem. Phys.*, **11**, 15,573–15,629.

Morrison, H., and A. Gettelman (2008), A new two-moment bulk stratiform cloud microphysics scheme in the Community Atmospheric Model (CAM3), Part I: Description and Numerical Tests, *J. Clim.,* **21,** 3642-3659.

Neale, R. B., et al. (2010), Description of the NCAR Community Atmosphere Model (CAM5.0), *NCAR/TN-486+STR*, NCAR, Boulder, Colo. [Available at http://www.cesm.ucar.edu/models/cesm1.0/cam/docs/description/cam5_desc.pdf.]

Niu, F., and Z. Li, (2012), Systematic variations of cloud top temperature and precipitation rate with aerosols over the global tropics, *Atmos. Chem. Phys.*, **12**, 8491–8498.

Ohara, T., H. Akimoto, J. Kurokawa, N. Horii, K. Yamaji, X. Yan, and T. Hayasaka (2007), An Asian emission inventory of anthropogenic emission sources for the period 1980–2020, *Atmos. Chem. Phys. Disc.*, **7**, 6843–6902.

Park, S., and C. S. Bretherton (2009), The University of Washington shallow convection and moist turbulence schemes and their impact on climate simulations with the Community Atmosphere Model, *J. Clim.*, **22**, 3449–3469.

Peng, C., X. Wu, G. Liu, T. Johnson, J. Shah, and S. Guttikunda (2002), Urban air quality and health in China, *Urban Stud,* **39(12),** 2283–2299.

Qian, Y., W. I. Gustafson, L. R. Leung, and S. J. Ghan (2009), Effects of soot-induced snow albedo change on snowpack and hydrological cycle in western United States based on Weather Research and Forecasting chemistry and regional climate simulations, *J. Geophys. Res.*, **114**(D03), 108, doi:10.1029/2008JD011039.

Rosenfeld, D., U. Lohmann, G. B. Raga, C. D. O'Dowd, M. Kulmala, S. Fuzzi, A. Reissell, and M. O. Andreae (2008), Flood or drought: How do aerosols affect precipitation? *Science*, **321**, 1309–1313.

Seifert, A., and K. D. Beheng (2006), A two-moment cloud microphysics parameterization for mixed-phase clouds: Part 2. Maritime vs. continental deep convective storms, *Meteorol. Atmos. Phys*., **92**, 67–82, doi:10.1007/s00703-005-0113-3.

Skamarock, W. C., J. B. Klemp, J. Dudhia, D. O. Gill, D. M. Barker, M. G. Duda, X.- Y. Huang, W. Wang, and J. G. Powers (2008), A description of the Advanced Research WRF Version 3, *NCAR Tech. NoteTN- 475+STR*, 88 pp., Natl. Cent. for Atmos. Res., Boulder, Colo.

Song, X., and G. J. Zhang (2011), Microphysics parameterization for convective clouds in a global climate model: Description and single- column model tests, *J. Geophys. Res.,* **116,** D02201, doi:10.1029/2010JD014833.

Song, X., G. J. Zhang, and J.-L. F. Li (2012), Evaluation of microphysics parameterization for convective clouds in the NCAR Community Atmosphere Model CAM5, *J. Clim.*, **25,** 8568-8590.

Streets, D. G., T. C. Bond, G. R. Carmichael, S. D. Fernandes, Q. Fu, D. He, Z. Klimont, S. M. Nelson, N. Y. Tsai, M. Q. Wang, J.-H. Woo, and K. F. Yarber (2003), An inventory of gaseous and primary aerosol emissions in Asia in the year 2000, *J. Geophys. Res.*, **108(D21),** 8809, doi:10.1029/2002JD003093.

Streets, D. G., J. Hao, Y. Wu, J. Jiang, M. Chan, H. Tian, and X. Feng (2005), Anthropogenic mercury emissions in China, *Atmos. Environ.*, **39,** 7789–7806.

Tao, W.-K., X. Li, A. Khain, T. Matsui, S. Lang, and J. Simpson (2007), Role of atmospheric aerosol concentration on deep convective precipitation: Cloud-resolving model simulations, *J. Geophys. Res.*, **112**, D24S18, doi:10.1029/2007JD008728.

Tao, W.-K., J.-P. Chen, Z. Li, C. Wang, and C. Zhang (2012), Impact of aerosols on convective clouds and precipitation, *Rev. Geophys.,* **50,** RG2001, doi:10.1029/2011RG000369.

van den Heever, S. C., G. G. Carrio, W. R. Cotton, P. J. DeMott, and A. J. Prenni (2006), Impact of nucleating aerosol on Florida storms, part 1: Mesoscale simulations, *J. Atmos. Sci.*, **63**, 1752–1775

van den Heever, S. C., G. L. Stephens, and N. B. Wood (2011), Aerosol indirect effects on tropical convection characteristics under conditions of radiative-convective equilibrium, *J. Atmos. Sci.,* **68,** 699–718, doi:10.1175/2010JAS3603.1.

Wang, C. (2005), A modeling study of the response of tropical deep convection to the increase of cloud condensation nuclei concentration: 1. Dynamics and microphysics, *J. Geophys. Res.,* **110,** D21211, doi:10.1029/2004JD005720.

Wu, L., H. Su, and J. H. Jiang (2013), Regional simulation of aerosol impacts on precipitation during the East Asian summer monsoon, *J. Geophys. Res.,* **118,** 6454–6467, doi:10.1002/jgrd.50527.

Xu, Q. (2001), Abrupt change of the mid-summer climate in central east China by the influence of atmospheric pollution, *Atmos. Environ.,* **35**, 5029 – 5040.

Yang, B., and Coauthors (2013), Uncertainty quantification and parameter tuning in the CAM5 Zhang-McFarlane convection scheme and impact of improved convection on the global circulation and climate, *J. Geophys. Res. Atmos*., **118,** 395–415, doi:10.1029/2012JD018213.

Yang, Q., and Coauthors (2012), Impact of natural and anthropogenic aerosols on stratocumulus and precipitation in the Southeast Pacific: a regional modelling study using WRF-Chem, *Atmos. Chem. Phys.,* **12,** 8777-8796, doi:10.5194/acp-12-8777- 2012.

Young, K. C. (1974), The role of contact nucleation in ice phase initiation in clouds, *J. Atmos. Sci.*, **31**, 768–776.

Zaveri, R. A., and L. K. Peters (1999), A new lumped structure photochemical mechanism for large-scale applications, *J. Geophys. Res.*, **104**, 30,387–30,415.

Zhang, G. J., and N. A. McFarlane (1995), Sensitivity of climate simulations to the parameterization of cumulus convection in the Canadian Climate Centre General Circulation Model, *Atmos. Ocean*, **33**, 407–446.

Zhang, R., G. Li, J. Fan, D. L. Wu, and M. J. Molina (2007), Intensification of Pacific storm track linked to Asian pollution, *Proc. Natl. Acad. Sci. U. S. A.,* **104,** 5295–5299, doi:10.1073/pnas.0700618104.

Zhang, Y., J.-P. Huang, D. K. Henze, and J. H. Seinfeld (2007), The Role of Isoprene in Secondary Organic Aerosol Formation on a Regional Scale, *J. Geophys. Res.*, **112,** D20207, doi:10.1029/2007JD008675.

Zhang, Y., X.-Y. Wen, and C. J. Jang (2010), Simulating Climate-Chemistry-Aerosol-Cloud-Radiation Feedbacks in Continental U.S. using Online-Coupled WRF/Chem, *Atmos. Environ.*, **44**(29), 3568-3582.

Zhang, Y., Y.-C. Chen, G. Sarwar, and K. Schere (2012), Impact of Gas-Phase Mechanisms on WRF/Chem Predictions: Mechanism Implementation and Comparative Evaluation, *J. Geophys. Res.,* **117**, D1, doi:10.1029/2011JD015775.

Zhang, Y., K. Sartelet, S. Zhu, W. Wang, S.-Y. Wu, X. Zhang, K. Wang, P. Tran, and C. Seigneur (2013), Application of WRF/Chem-MADRID and WRF/Polyphemus in Europe, Part II: Evaluation of Chemical Concentrations, Sensitivity Simulations, and Aerosol-Meteorology Interactions, *Atmos. Chem. Phys.,* **13**, 6845-6875, 2013.

Zhao, C., X. Liu, L. R. Leung, and S. Hagos (2011), Radiative impact of mineral dust on monsoon precipitation variability over West Africa, *Atmos. Chem. Phys*, **11**, 1879–1893.

Zhao, C., X. Liu, and L. R. Leung (2012), Impact of the Desert dust on the summer monsoon system over Southwestern North America, *Atmos. Chem. Phys*, **12**, 3717–3731.

Table 1. Statistical skill scores of pattern correlation (PC), bias (BIAS), and root mean square error (RMSE) for the simulated spatial disribution of accumulated surface precipitation (PRC_S) and time series of domain-averaged surface rain rate (PRC_T) and shortwave radiative fluxes at the surface (RAD_T) using the observation of TMPA for precipitation and CERES for radiative fluxes data. The values in the parenthesis of PRC_S and PRC_T are calcuated using the CMA data and the values in parenthesis of RAD_T are for the longwave radiation at the top of atmosphere. Comparing the statistical skill scores between MP and NOMP, better results of MP over NOMP are marked in bold type.

	PRC_S			PRC_T			RAD_T		
	PC	BIAS	RMSE	PC	BIAS	RMSE	PC	BIAS	RMSE
MP	**0.36**	**-18.88**	**103.52**	**0.42**	**-0.07**	**0.58**	**0.71**	**-9.33**	**23.57**
	(**0.30**)	(30.79)	(**103.69**)	(**0.39**)	(0.13)	(**0.52**)	(0.61)	(**2.59**)	(**15.85**)
NOMP	0.19	-42.05	121.65	0.25	-0.17	0.67	0.59	17.15	26.58
	(0.20)	(**7.69**)	(106.13)	(0.37)	(**0.03**)	(**0.52**)	(**0.65**)	(-7.01)	(16.12)

Table 2. List of symbols used in cloud microphysical budgets analysis in Figures 4c, 4c, and 4f.

Symbol	Description
Pracs	Production rate for accretion of rain by snow
Pracw	Production rate for accretion of cloud water by rain
Praut	Production rate for auto-conversion of cloud water to form rain
Prevp	Production rate for evaporation of rain
Prfrz	Prodiction rate for heterogeneous freezing of rain to snow
Prsed	Production rate for sedomentation of rain
Psaci	Production rate for accretion of cloud ice by snow
Psacw	Production rate for accretion of cloud water by snow
Psaut	Production rate for auto-conversion of cloud ice to form snow
Pssed	Production rate for sedomentation of snow

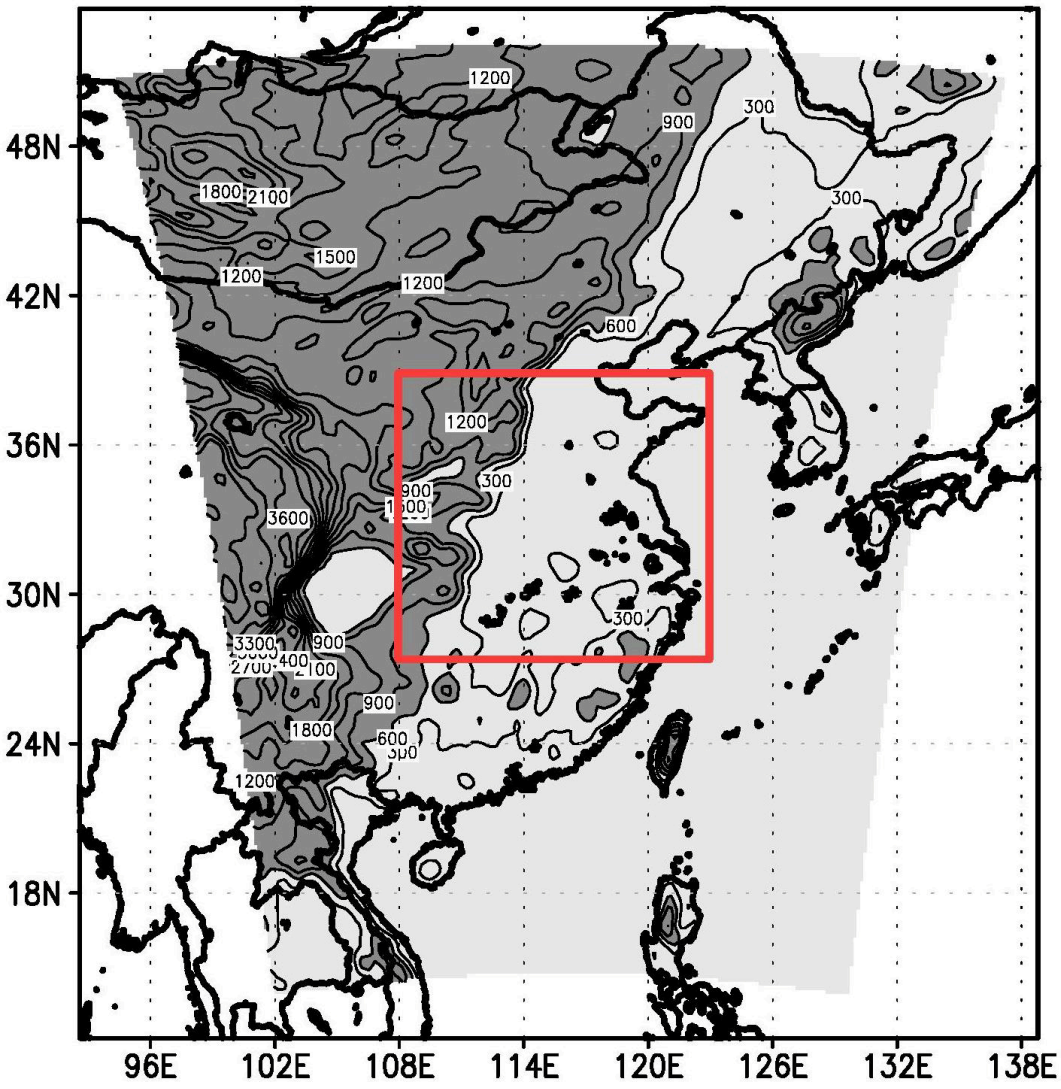

Figure 1. Model domain with terrain heights contoured every 300 m. Terrain heights higher than 600 m are shaded. The red box indicates the analysis domain.

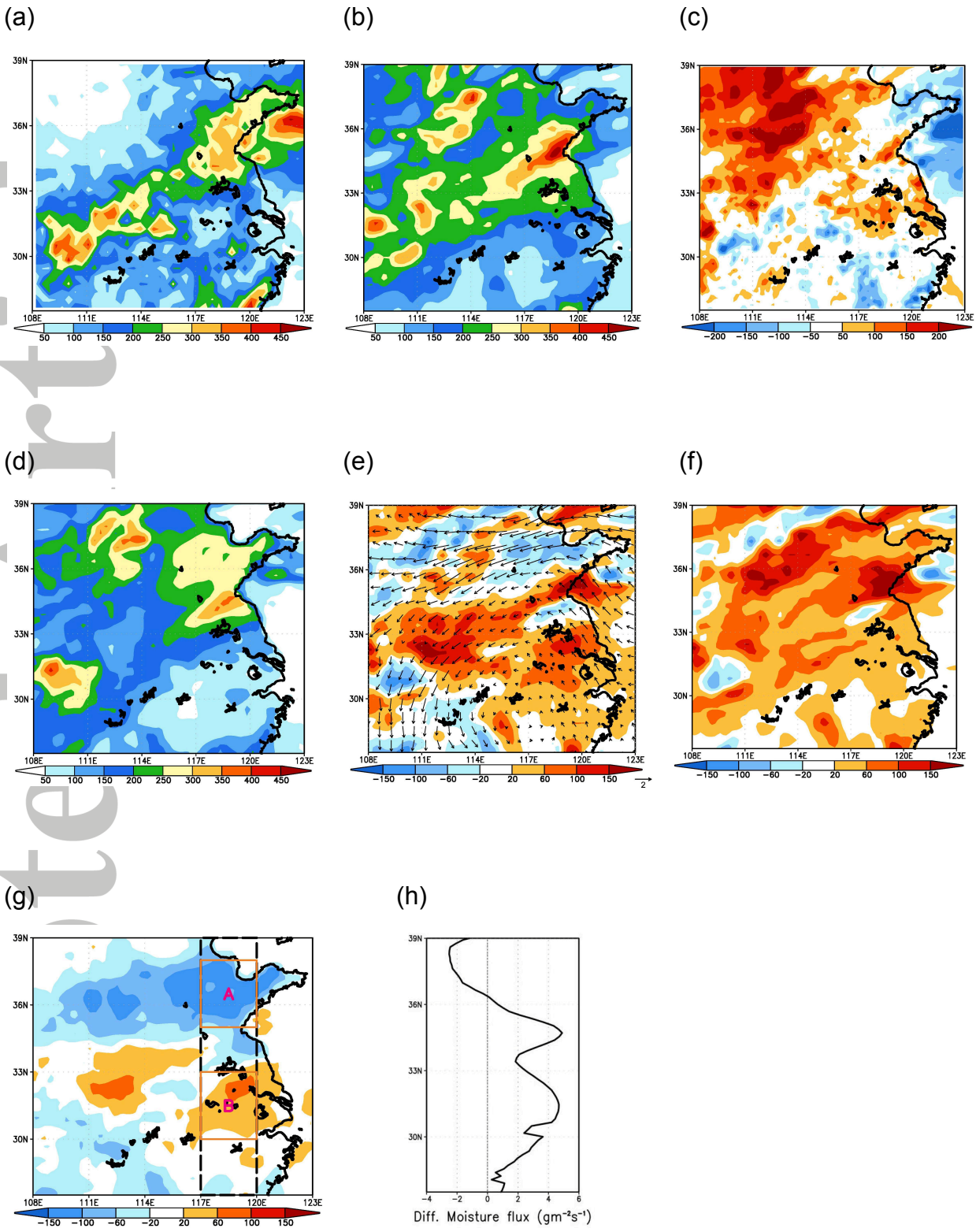

Figure 2. Accumulated surface precipitation [unit: mm] during July 2008 from the (a) China Merged precipitation Analysis (CMA) data and (b) MP. (c) represents the difference in total accumulated surface precipitation between experiments (MP

minus CMA). (d) is the same as (b) but for NOMP. (e) represents the difference in total accumulated surface precipitation (shaded) and time-averaged wind fields at 850 mb (vector) between experiments (MP minus NOMP). (f) and (g) represent the differences in the grid-resolved precipitation and the paramerterized cumulus precipitation, respectively. Difference of zonally averaged moisture flux [unit: g m^{-2} s^{-1}], a product of water vapor mass and meridional wind averaged over the lower atmosphere from surface to 2 km is shown in Figure 2h. The region for averaging is marked by the black-dashed rectangular box in Fig. 2g.

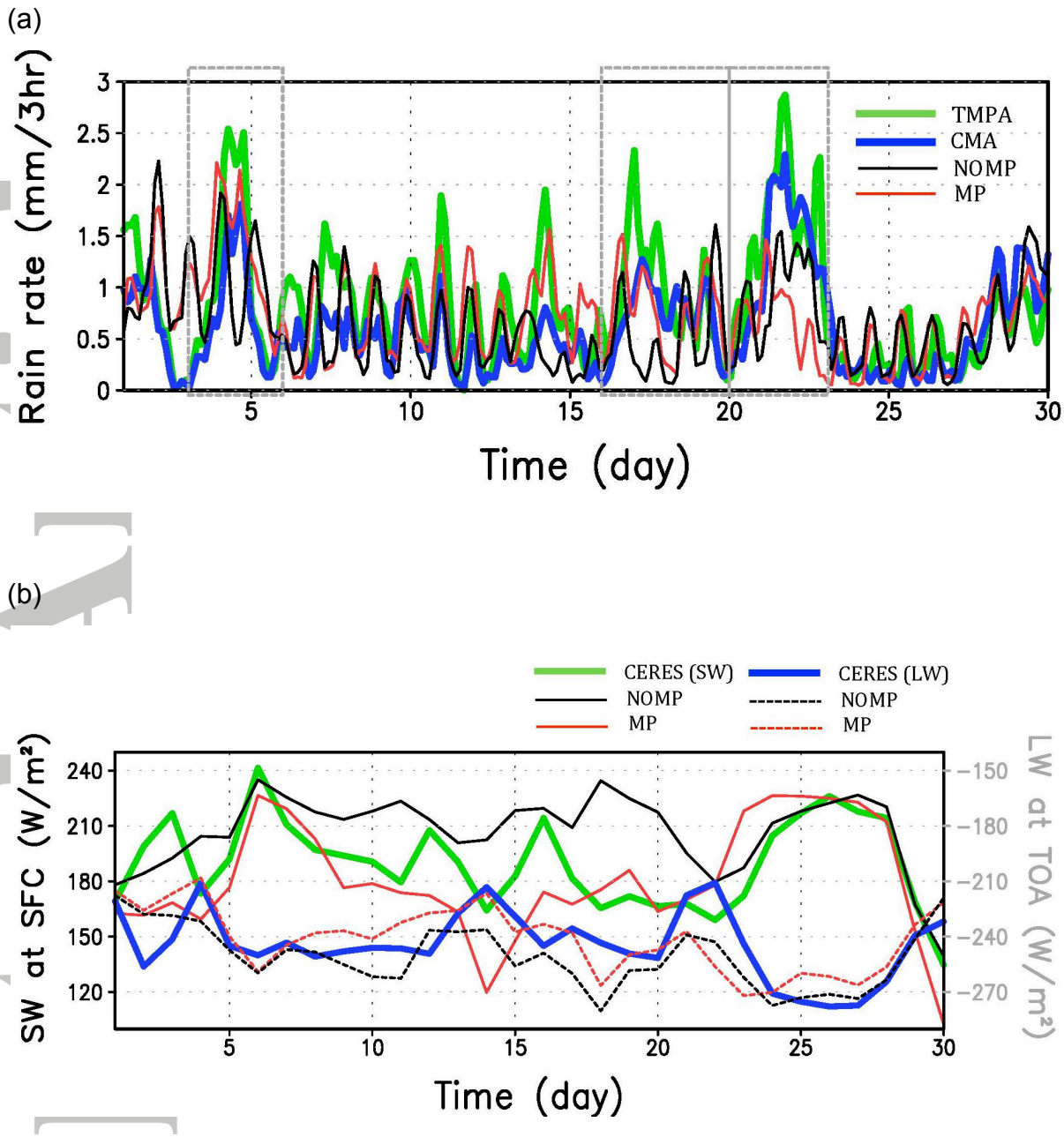

Figure 3. Time series of (a) domain-averaged surface rain rate [unit: mm $3h^{-1}$] and (b) daily-averaged surface net shortwave (SW) flux and outgoing longwave (LW) flux [unit: W m^{-2}] at the top of atmosphere from observation (green line for SW and blue line for LW), NOMP (black line), and MP (red line). In Fig. b, the simulated LW flux is drawn in dotted lines and positive (negative) values denote downward (upward) radiative fluxes. The three dotted boxes in Figure 3a indicate the heavy precipitation periods. The horizontal resolutions of CMA, TMPA, and CERES data are $0.1°$,$0.25°$, and $1.0°$, respectively.

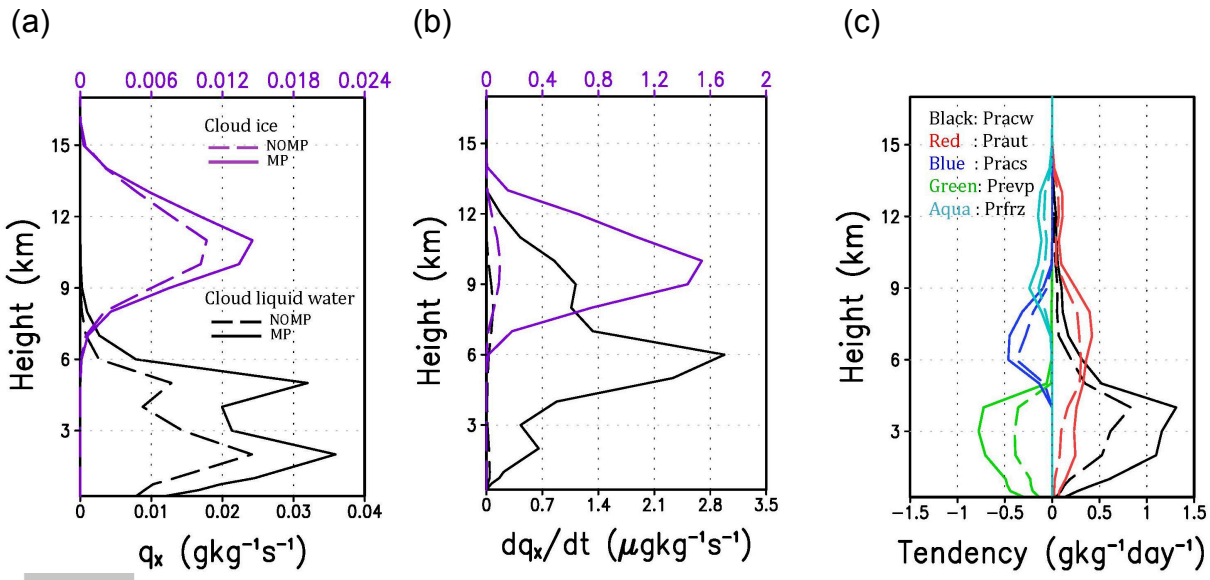

Figure 4. Vertical profiles of time- and domain-averaged (a) total mixing ratios of cloud ice and cloud liquid water and (b) detrained rates of cloud ice and cloud liquid water mass from the ZM cumulus scheme. (c) represents the contribution of several microphysics processes for rain mass production in the startiform microphyscis. In all figures, solid lines denote results from MP and dashed lines from NOMP. Cloud ice mass in Figures 4a and 4b are drawn in purple color. The list of symbols used to describe the cloud microphysical budget analysis in Figure 4c is provided in Table 2.

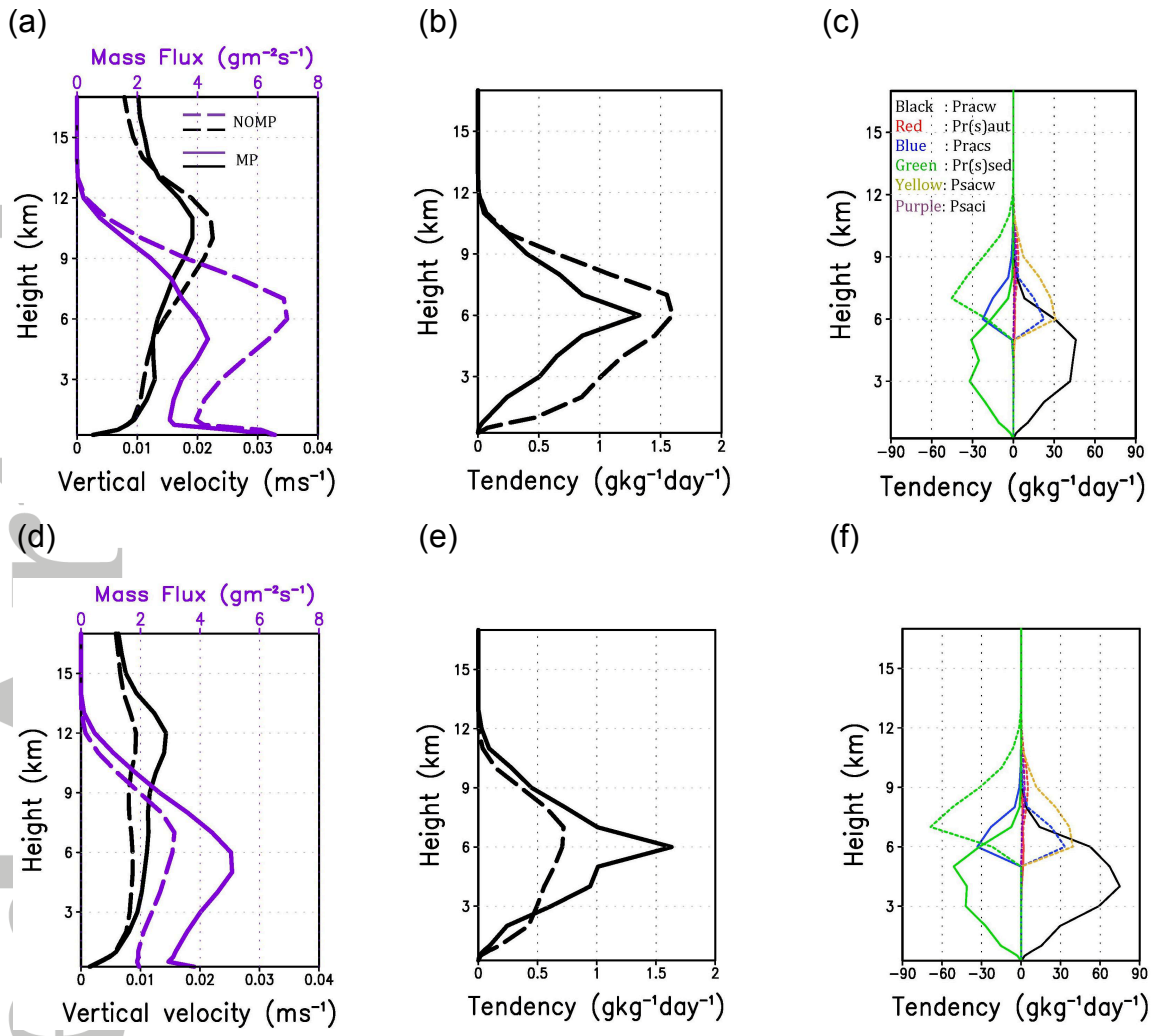

Figure 5. Vertical profiles of (a) time- and domain-averaged net convective mass flux (purple line), calculated by combination of updraft and downdraft mass fluxes and upward vertical velocity (black line) from MP (solid line) and NOMP (dashed line). The lines in (b) indicate the time domain-averaged cumulus precipitation production rate. (c) is for the contribution of several microphysics processes in the cumulus parameterization for rain and snow mass production in MP. All quantities shown in Figures 5a-c are averaged over the sub-domain A (35-38 N, 117-120 E), marked by the orange rectangular box in Figure 2g. The lower panels show the same as the upper panels but for averages over the sub-domain B (30-33 N, 117-120 E). In Figs. 5c and f, source/sink terms for rain mass are drawn with solid line and those for snow mass are drawn with dotted line. The list of symbols used to describe the cloud microphysical budget analysis in Figures 5c and f is provided in Table 2.

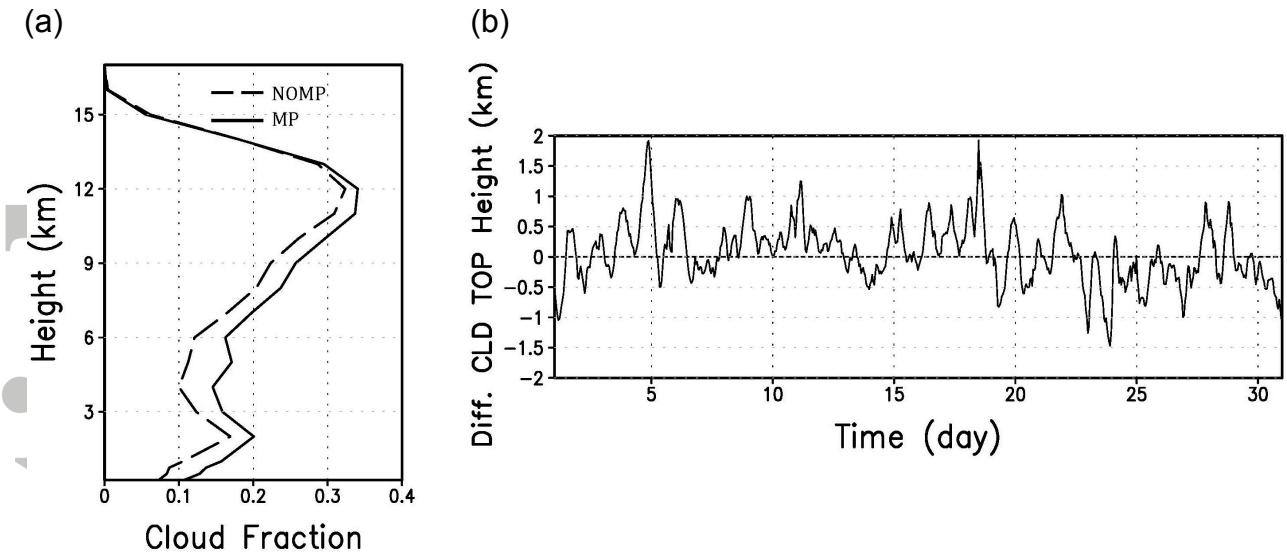

Figure 6. (a) The time- and domain-averaged total cloud fraction from MP and NOMP and (b) the difference in time series of domain-averaged cloud top height between the experiments (MP minus NOMP). Cloud top is defined as the highest level where cloud ice mass exceeds at least 10^{-5} kg kg^{-1}.

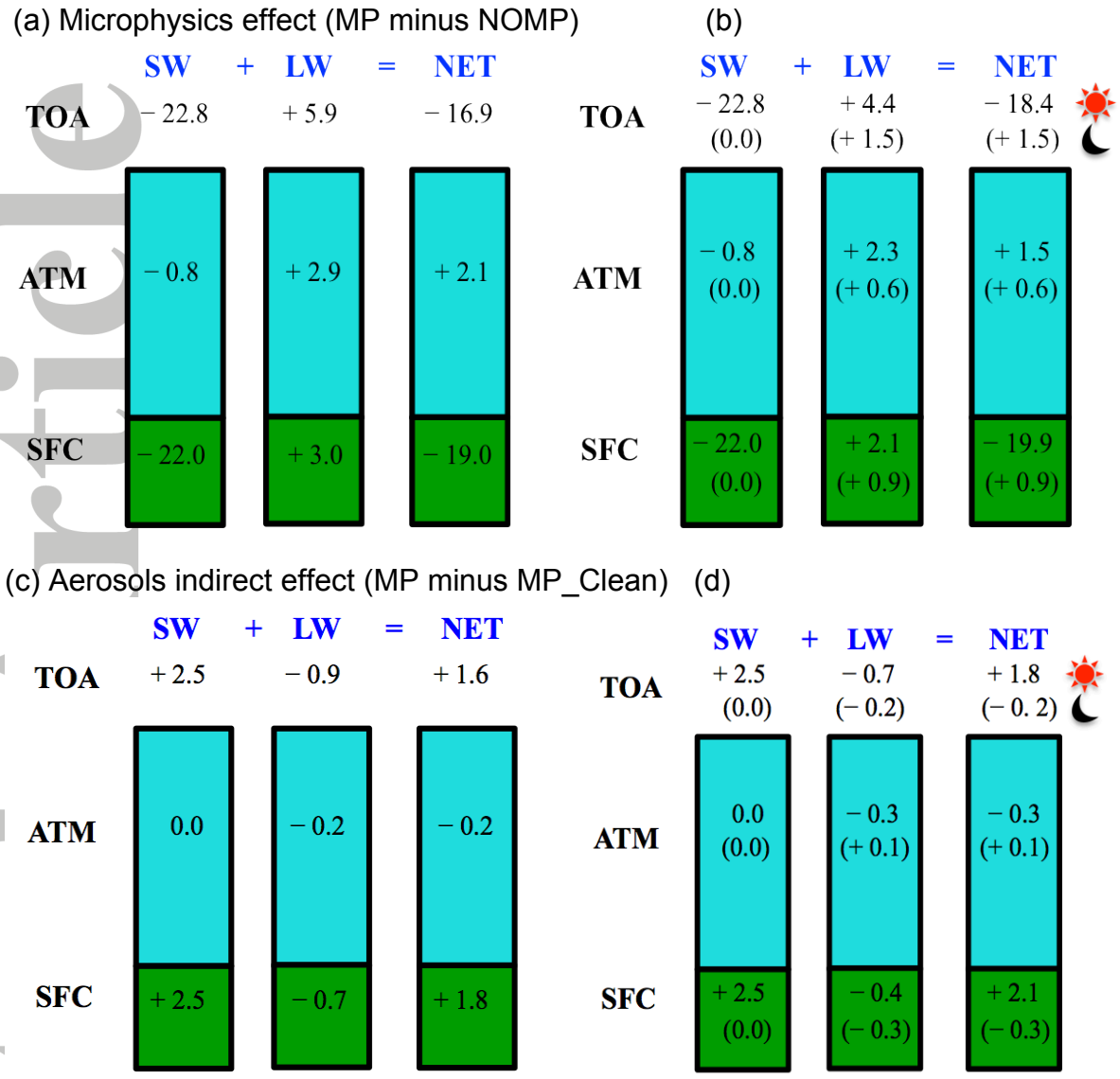

Figure 7. SW, LW, and net radiative cloud forcing caused by microphysics effect in the ZM cumulus scheme (MP minus NOMP) (a and b) and aerosol effect (MP minus MP_Clean) (c and d) at the top of atmosphere (TOA), atmosphere (ATM), and surface (SFC). (a) and (c) are drawn for the whole time period and (b) and (d) are for daytime and nighttime (the values in the parentheses are for nighttime).

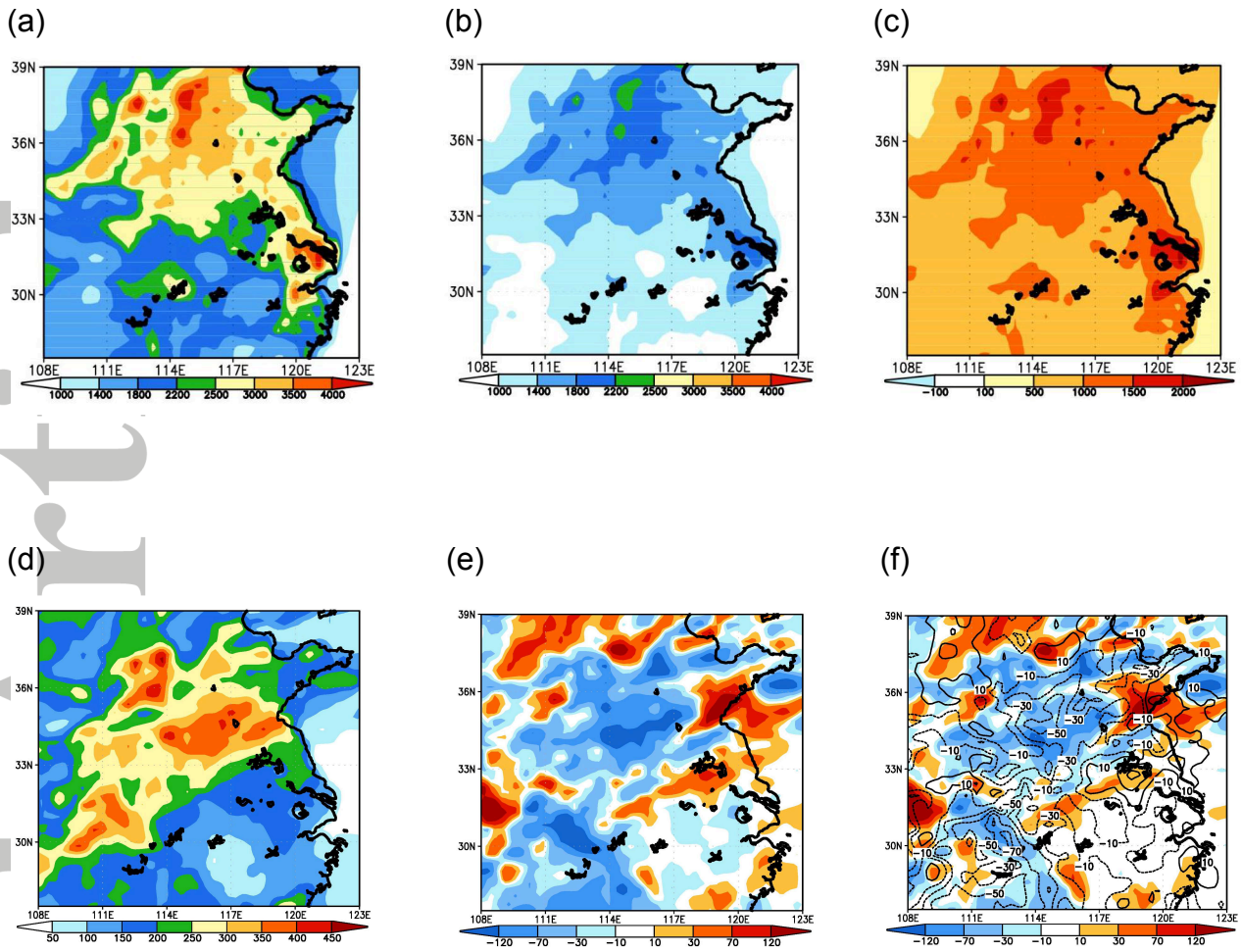

Figure 8. Time-averaged aerosol number concentrations [unit: cm^{-3}] during July 2008 from (a) MP and (b) MP_Clean. (c) represents the difference in aerosol number concentrations between the experiments (MP minus MP_Clean). (d) is for total accumulated surface precipitation [unit: mm] from MP_Clean and the difference in accumulated surface precipitation (MP minus MP_Clean) is shown in (e). (f) shows the differences in the grid-resolved preciptiation (shaded) and cumulus precipitation (contour). For difference in cumulus preciptiation, solid (Dotted) lines, which are drawn with an interval of 20 mm starting at +10 (−10) mm, indicate the positive (negative) difference.

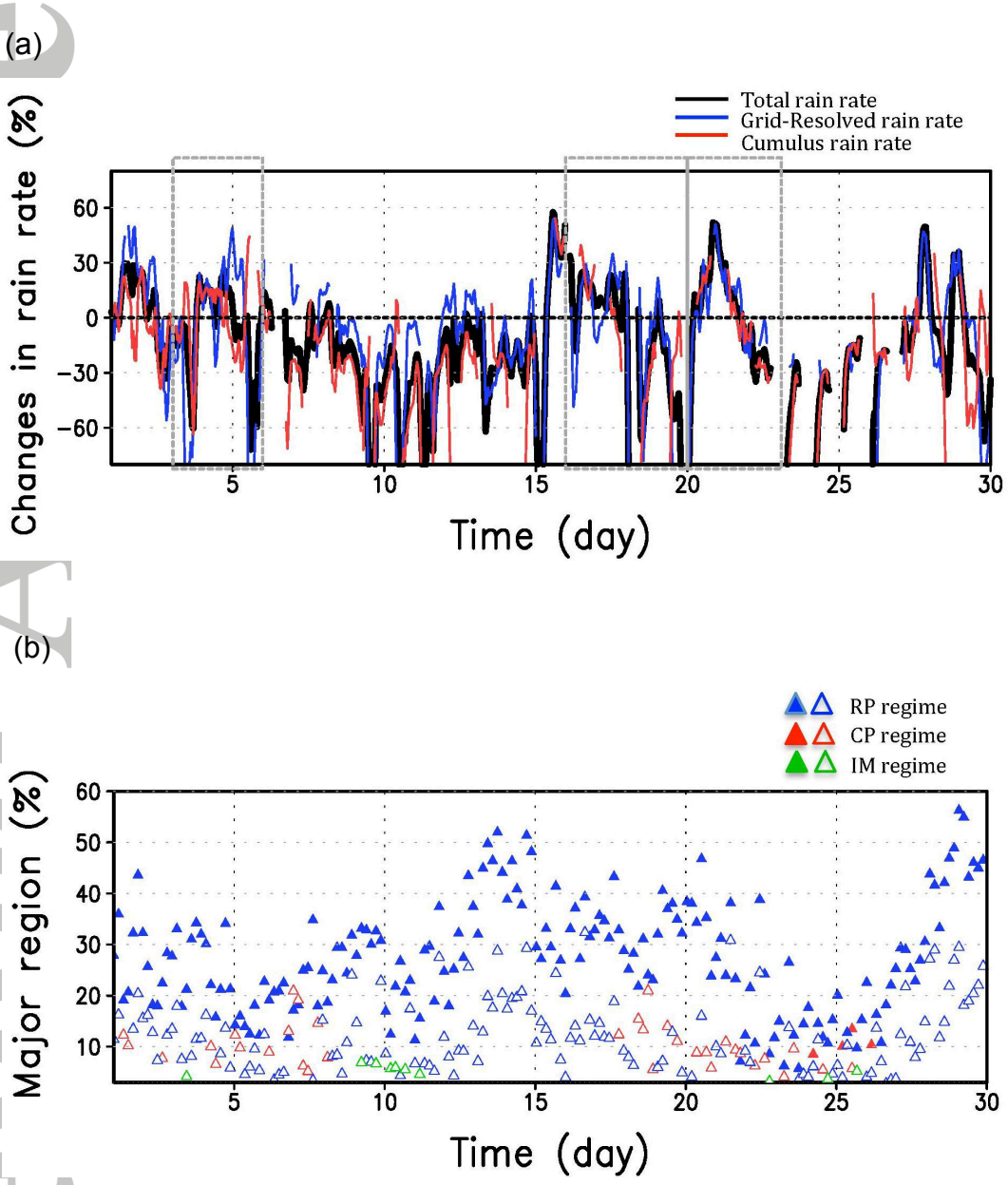

Figure 9. (a) The relative changes [unit: %] in total rain rate (black line), grid-resolved rain rate (blue line), and cumulus rain rate (red line) calculated as (100× (MP-MP_Clean) /MP_Clean). Here we use the threshold value of 0.05 mm h^{-1} to define a rain event. The three dotted boxes indicate the heavy precipitation periods. The dots in (b) indicate the most dominant precipitation regime for MP (closed triangle) and MP_Clean (open triangle) over the whole analysis domain. Blue indicates a grid-resolved precipitation dominant (RP) regime, red is for a cumulus precipitation domimant (CP) regime, and green is for an inter-mediate (IM) regime.

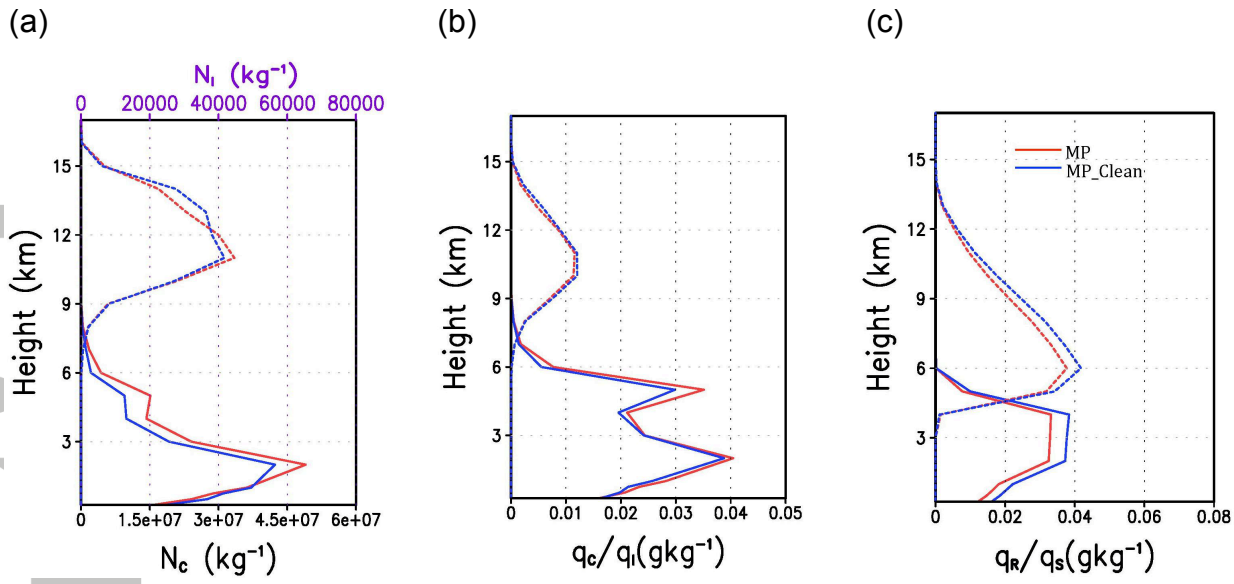

Figure 10. Vertical profiles of time- and domain-averaged (a) number concentrations, (b) mixing ratios of cloud liquid water and ice, and (c) mixing ratios of rain and snow from MP (red line) and MP_Clean (blue line). Here, quantities for ice particles are drawn with dotted lines. All variables are composited over the RP regime.

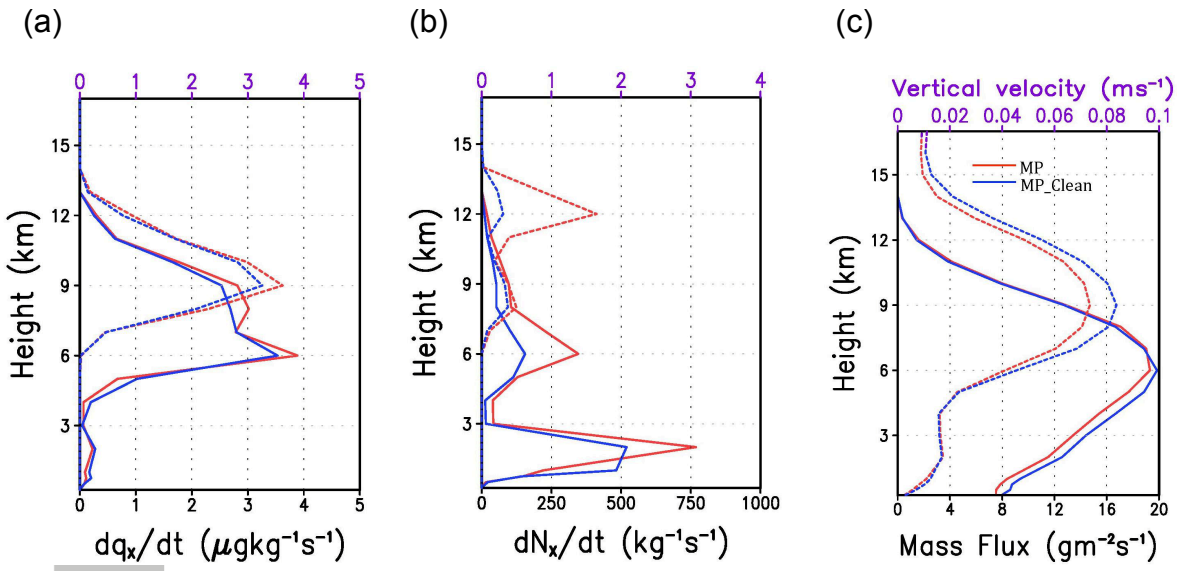

Figure 11. Vertical profiles of time- and domain-averaged detrained rates of (a) mixing ratios and (b) number concentrations of cloud liquid water (solid line) and cloud ice (dotted line) from the cumulus scheme, respectively. (c) is for net mass flux (solid line) and upward vertical velocity (dotted line) from MP (red line) and MP_Clean (blue line). The grid points in which the maximum vertical velocity is greater than 0.5 m s^{-1} within a column are selected for Fig. 11c. All variables shown here are composited over the CP regime.

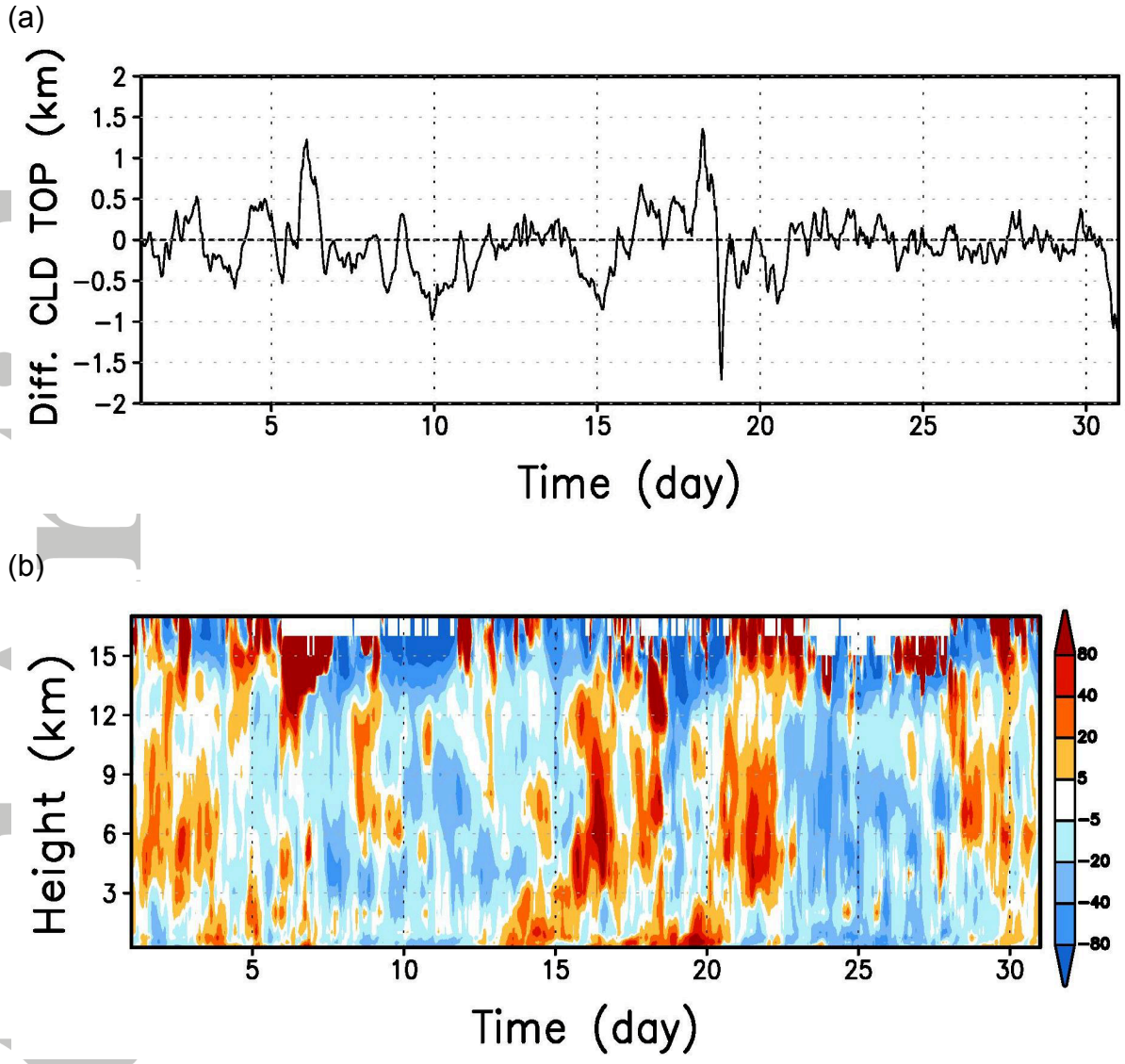

Figure 12. (a) The difference in time series of domain-averaged cloud top height between the experiments (MP minus MP_Clean) and (b) profile of the relative changes [unit: %] in time sereis of domain-averaged total cloud fraction calculated as (100× (MP-MP_Clean) /MP_Clean).

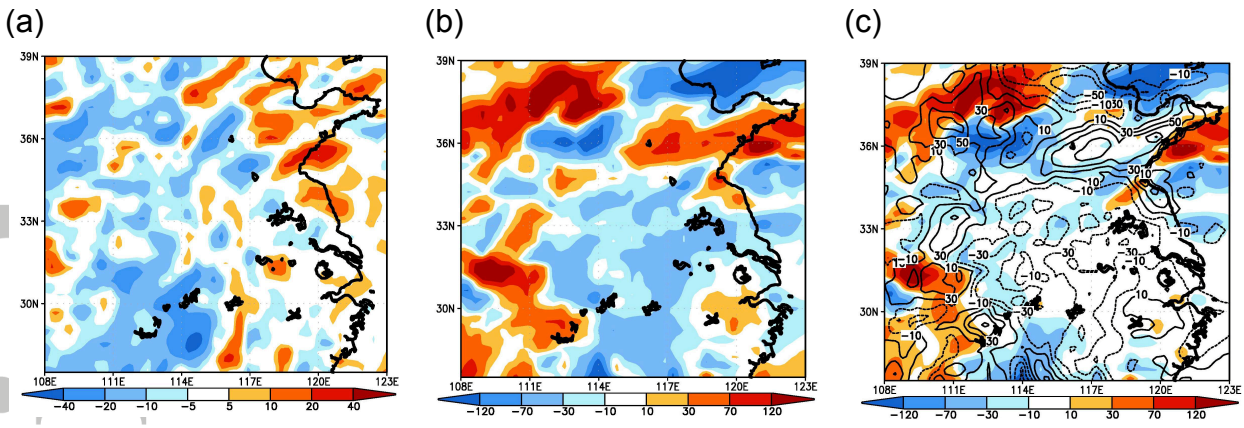

Figure 13. Differences in total accumulated surface precipitation [unit: mm] between (a) Ens_MP and Ens_MP_Clean (Ens_MP minus Ens_MP_Clean) and (b) NOMP and NOMP_Clean (NOMP minus NOMP_Clean). (c) shows the differences in the grid-resolved preciptiation from large-scale clouds (shaded) and cumulus precipitation from the parameterized cumulus clouds (contour) between NOMP and NOMP_Clean.